

# Investigation of the Gas-Phase Structures of Fucosylated Glycans Employing Cold-Ion Infrared Spectroscopy

Master Thesis  
Freie Universität Berlin

Accomplished at the Molecular Physics Department  
of the Fritz Haber Institute  
October 2017 to April 2018

Maïke Lettow

First Examiner      Prof. Dr. Kevin Pagel  
Second Examiner    Prof. Dr. Christoph Schalley

Freie Universität Berlin

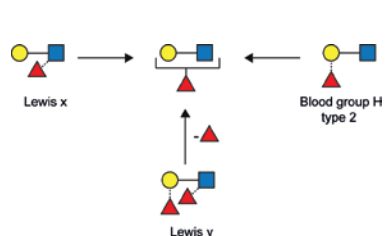


Fritz-Haber-Institut der  
MAX-PLANCK-GESELLSCHAFT



## ABSTRACT

Glycans have essential structural and functional roles in living organisms and at the same time represent the most complex class of biomolecules, which makes their analysis critical yet extremely challenging. Fucose is a deoxy monosaccharide that is linked to every fourth non-reducing end in mammalian glycans. In mass spectrometry, fucose migration is a reoccurring issue that can lead to false sequence assignments. The reaction involves an intramolecular transfer of a fucose monosaccharide to adjacent or remote sites. In preceding research, fucose migration was observed in glycan fragments produced by collision-induced dissociation in tandem mass spectrometry and was strictly associated with the fragmentation process. Comparable to the investigation of peptide scrambling in the early 2000's, multidimensional approaches are needed to shed light on the reaction. In this work, cold-ion infrared spectroscopy and ion mobility-mass spectrometry are employed to investigate the gas-phase structures of fucosylated glycans of biological relevance. The results show that fucose migration reactions can occur in intact glycan ions independent of fragmentation. Two intact trisaccharides as well as a fragmented tetrasaccharide rearrange to the same chemical structure. A mobile proton located at the amide functional group is likely to catalyze the reaction in these molecules. The results obtained from an in-source activation experiment as well as from utilizing a cooled ion trap suggest an interconversion to one of the trisaccharides. The observation indicates a possible low-energy barrier for this migration reaction and



generalizes fucose migration to an issue that may universally occur in mass spectrometry experiments.

Figure 1: Schematic illustration of the observed fucose migration reaction.

## ACKNOWLEDGEMENTS

An dieser Stelle möchte ich mich bei Prof. Kevin Pagel und Prof. Gert von Helden bedanken, dass sie mich in ihre Arbeitsgruppen sehr herzlich aufgenommen haben. Von Prof. Kevin Pagel erhielt ich viele interessante Fragestellungen sowie neue Denkanstöße und Ideen. Prof. Gert von Helden sowie auch Prof. Gerard Meijer danke ich insbesondere für die Nutzung der Instrumente am Fritz-Haber-Institut der Max-Planck-Gesellschaft, ohne die ich meine Arbeit nicht hätte anfertigen können. Außerdem bedanke ich mich bei Prof. Kevin Pagel und bei Prof. Christoph Schalley für die Begutachtung der Masterarbeit.

Mein besonderer Dank gilt Eike Mucha. Er hat mich mit viel Geduld und großer Genauigkeit sowohl in allen Teilen der praktischen Arbeiten als auch beim Schreiben unterstützt. Die Einarbeitung in das Kalt-Ionen Infrarot Spektroskopie Experiment ist zeitaufwendig und trotzdem hatte ich das Gefühl, dass mit jeder meiner Fragen Raum und Zeit für Diskussionen entstand. Für die Unterstützung während der langen Messzeiten möchte ich mich neben Eike Mucha auch besonders bei Daniel A. Thomas, Ph.D. bedanken, der mich oft bei kniffligen Problemen unterstützte.

Des Weiteren möchte ich mich bei Christian Manz und Waldemar Hoffmann herzlich bedanken. Christian Manz danke ich für die Einarbeitung in die Ionenmobilitätsmassenspektrometrie und die Bereitstellung zusätzlicher Proben. Waldemar Hoffmann danke ich für die sofortige Bereitschaft, weitere Messungen zu übernehmen, die zu spannenden Ergebnissen führten. Weiterhin bedanke ich mich bei Prof. Mateusz Marianski für die ersten theoretischen Ergebnisse und guten Diskussionen. Bei Dr. Wieland Schöllkopf und Sandy Gewinner bedanke ich mich für ihre Arbeit am Freien-Elektronen-Laser des Fritz-Haber-Instituts und die vielen,

mal mehr, mal weniger genutzten Photonen. Außerdem möchte ich mich bei Dr. Fabian Pfrengle und Deborah Senf sowie auch Prof. Peter H. Seeberger vom Max-Planck-Institut für Kolloid- und Grenzflächenforschung in Potsdam für die Bereitstellung interessanter Proben bedanken.

Auch allen weiteren Mitgliedern beider Arbeitsgruppen und der gesamten Abteilung Molekülphysik des Fritz-Haber-Instituts danke ich für die gute Atmosphäre und ständige Hilfsbereitschaft. Ich bedanke mich für alle fachlichen und nicht-fachlichen Gespräche sowie auch für den einen oder anderen gemeinsamen Abend. Besonders bedanke ich mich bei Dr. Johanna Hofmann, Márkó Grabarics, Dr. Melanie Göth, Rayoon Chang, Suzan Almeida Dias Miranda, Jongcheol Seo, Ph.D., Xiao Jakob Schmidt, Henrik Haak, Sreekanta Debnath, Harald Knorke und Stefan Schlichting.

Zu guter Letzt bedanke ich mich bei meiner Familie und meinen Freunden für die persönliche Unterstützung und den familiären Rückhalt.

# TABLE OF CONTENTS

<b>1</b>	<b>Introduction .....</b>	<b>1</b>
<b>2</b>	<b>Fundamentals .....</b>	<b>4</b>
2.1	Chemical Structure of Glycans.....	4
2.2	Role of Fucosylated Glycans.....	8
2.3	Investigated Glycans.....	9
2.4	Fucose Migration in Mass Spectrometry — Status Quo.....	10
2.5	Infrared Spectroscopy of Glycans in the Gas Phase .....	17
<b>3</b>	<b>Experiments .....</b>	<b>21</b>
3.1	Cold-Ion Infrared Spectroscopy .....	21
3.2	Ion Mobility-Mass Spectrometry .....	26
3.3	Preparation of Samples.....	30
<b>4</b>	<b>Fucose Migration — A Universal Phenomenon in Mass Spectrometry.....</b>	<b>32</b>
4.1	Cold-Ion Infrared Spectroscopy of Fucosylated Glycan Ions.....	32
4.1.1	Sodium Adduct Ions.....	33
4.1.2	Protonated Ions .....	38
4.1.3	Ammonium Adduct Ions.....	46
4.1.4	Alkyl Ammonium Adduct Ions.....	50
4.1.5	Hydrogen-Deuterium Exchange Experiment .....	52
4.1.6	Precooled Glycan Ions .....	53
4.2	Ion Mobility-Mass Spectrometry .....	56
4.2.1	IM-MS Results .....	56
4.2.2	Probing Soft In-Source Activation .....	61
<b>5</b>	<b>Conclusion and Outlook .....</b>	<b>64</b>
<b>6</b>	<b>References .....</b>	<b>VI</b>
<b>7</b>	<b>Appendix .....</b>	<b>XI</b>

## LIST OF ABBREVIATIONS

ATD	Arrival time distribution
BG-H	ABO blood group H antigen
CCS	Collision cross section
CID	Collision-induced dissociation
DT	Drift tube
FEL	Free-electron laser
FWHM	Full width at half maximum
HMO	Human milk oligosaccharides
HPLC	High-performance liquid chromatography
IM-MS	Ion mobility-mass spectrometry
IR	Infrared
IRL	Internal residue loss
IRMPD	Infrared multiphoton dissociation
L	Linker
Le	Lewis antigen
M	Molecule in adducts or ions
MS	Mass spectrometry
$m/z$	Mass-to-charge ratio
nESI	nano-electrospray ionization
SNFG	Symbol nomenclature for glycans
TOF	Time-of-flight

SI unit abbreviations and sum formulas with exact chemical meaning are generally used without further explanation. Adduct ions and protonated ions in MS experiments are abbreviated using the typical nomenclature. For example, a sodium ( $\text{Na}^+$ ) adduct of a molecule (M) is represented as  $[\text{M}+\text{Na}]^+$ . Three letter codes for monosaccharides are used as defined in symbol nomenclature for glycans (SNFG)<sup>[1]</sup>. One letter codes are only used for xylose (X) and arabinose linked to xylose (A).





# 1 INTRODUCTION

Glycans are among the most abundant biomacromolecules in living organisms and are essential in a variety of biological functions, such as cell-signaling and molecular recognition.<sup>[2-4]</sup> In addition, glycosylation patterns of proteins, lipids or other organic molecules are in many cases highly dynamic which is obvious in an evolutionary sense<sup>[5]</sup> but also accounts for physiological variations as well as pathological variations<sup>[6]</sup>. In spite of these indispensable functions in biological processes, the immense structural complexity of glycans has significantly hindered the elucidation of glycan structure and function. The Utrecht University strikingly stated *via* their educational YouTube Channel: “Glycans are to biology what dark matter is to the universe: omnipresent and vital to fully understand it, yet shrouded in mystery.”<sup>[7]</sup>

As the third “-omics” discipline, glycomics follows the steps of proteomics and genomics. The field of glycomics, the systematic elucidation of all glycan structures, has advanced rapidly in recent years, and new methodologies are being developed to yield both high-resolution and high-throughput solutions. However, in contrast to proteomics<sup>[8]</sup> and genomics<sup>[9]</sup>, a “gold standard” method has not yet been identified. In general, the analysis of glycan sequence consists of three steps: isolation, identification and quantification. Mass spectrometry, as a whole, certainly has a key role in the sequence analysis of glycans<sup>[10-12]</sup>, comparable to its role in proteomics<sup>[13]</sup>.

In the early days of proteomics, a gas-phase rearrangement reaction was observed which led to erroneous sequence assignments. Peptide scrambling in protonated or multiply protonated b-type peptide ions involves head-to-tail macrocyclization and reopening reactions prior to fragmentation in tandem mass spectrometry with collision-induced dissociation (CID). As a consequence, the original sequence

information is lost. The phenomenon was first reported by Vachet, *et al.*<sup>[14]</sup> in 1997. Since the 2000s, the underlying mechanism and the structure of the macrocyclic intermediate have been successfully investigated with tandem mass spectrometry<sup>[15-19]</sup>, isotopic labelling, ion mobility-mass spectrometry (IM-MS)<sup>[20-21]</sup>, hydrogen deuterium exchange, infrared (IR) spectroscopy and computational modeling<sup>[22-24]</sup>. It has been found that the incidence of this gas-phase rearrangement is negligible in shotgun proteomics but of major interest in understanding the fragmentation pathways in CID.<sup>[25-27]</sup>

A rearrangement reaction frequently observed in mass spectrometry of glycan ions is the intramolecular transfer of a terminal fucose, a deoxy monosaccharide that lacks a hydroxyl group at C-6, to adjacent or remote monosaccharides with subsequent internal residue loss. So far, this phenomenon has been observed during CID in tandem MS and was strictly associated with the fragmentation process. The rearrangement or migration reaction often leads to the presence of misleading fragment ions, which in turn can lead to erroneous structural assignments. The rearrangement reaction has been interchangeably termed internal residue loss (IRL), fucose migration or also hexose migration. The latter term is used for migration reactions of other monosaccharides, such as xylose, rhamnose or mannose. The wording clearly reflects the obscurity of the underlying mechanism. First descriptions of a glycan rearrangement reaction involving alditols were already reported by McNeil<sup>[28]</sup> in the 1980s. However, multidimensional investigations, similar to the research on peptide scrambling, are necessary to fully understand the prevailing phenomenon.

In this thesis, numerous methods are employed to gain a better understanding of fucose migration reactions. The main experiment combines MS and IR spectroscopy

of cold ions. In the experiment, glycans are softly ionized with nano-electrospray ionization (nESI), selected by their mass-to-charge ratio ( $m/z$ ) in a quadrupole and stored in a variable-temperature ion trap, which can be operated at room temperature or cooled stepwise to  $\sim 80$  K. Once stored in the ion trap, the ions are picked up by traversing superfluid helium nano-droplets and cooled to 0.4 K. Encapsulated in the droplets, the ions are irradiated with IR light supplied by the *Fritz Haber Institute (Berlin)* free-electron laser (FEL), ejected from the droplets and detected in a time-of-flight (TOF) mass analyzer. Measurement of the TOF ion signal as a function of the incident wavelength yields a highly resolved IR spectrum. The utility of this method for the identification of isomeric glycans up to tetrasaccharides has been shown recently.<sup>[29]</sup> Fingerprint spectra for glycans with minute structural and conformational variations can be obtained which identify them unambiguously. In this thesis, the method is used to investigate different tri- and tetrasaccharides as well as the impact of different adduct ions on fucose migration reactions. Hydrogen-deuterium exchange and variable-temperature ion trapping experiments are performed to further aid structural assignment. Additionally, IM-MS is employed to investigate the gas-phase structure of fucosylated glycans. It has been shown recently that IM-MS can be used to separate, with some restrictions, structurally related fucosylated glycans by their gas-phase shapes, quantified by the measurement of collision cross sections (CCS).<sup>[30]</sup> The CCS of model fucosylated glycans are utilized in this work to corroborate results from the cold-ion IR spectroscopy experiments as well as to investigate the role of in-source activation in fucose migration.

## 2 FUNDAMENTALS

### 2.1 CHEMICAL STRUCTURE OF GLYCANS

Glycans are defined by IUPAC recommendations as a large number of glycosidically linked monosaccharides, commonly more than ten.<sup>[31]</sup> More generally, the term glycans is interchangeably used with the terms carbohydrates, sugars or saccharides. The most basic units are monosaccharides. Disaccharides are composed of two monosaccharide units and oligosaccharides of more than three. Polysaccharides are defined as a synonym to glycans. Historically, carbohydrates or the hydrates of carbons are represented by the empirical formula  $C_n(H_2O)_m$ . As known today, many naturally occurring carbohydrates are exceptions from the former chemical representation, e.g. deoxyhexoses.

Monosaccharide families are the aldoses and ketoses consisting of an aldehyde function or a ketone function, respectively, which can be further grouped by their number of containing carbon atoms from trioses to hexoses. The carbon atoms are labelled numerically beginning with the carbon atom of the aldehyde at C-1 position or next to the ketone function at C-2 position towards the chain. The orientation of the hydroxyl groups in the chain defines the different isomers. The D- or L-configuration is defined by the orientation of the hydroxyl group at the stereocenter furthest from the highest oxidized carbon atom. In Figure 2, the D- and L-configuration are shown for a biologically relevant monosaccharide. Monosaccharides that differ in only one stereocenter are called epimers.

Generally, monosaccharides can be present in an open chain form or in two different heterocyclic ring forms. Five-membered rings are called furanoses and the usually preferred six-membered rings pyranoses. In the heterocyclic ring forms,

another stereogenic center, the anomeric center, is created by a ring-closing reaction. The two possible configurations are termed alpha ( $\alpha$ ) and beta ( $\beta$ ) anomers, according to the relative orientation at the anomeric center and the highest, chiral carbon atom in the ring, the anomeric reference atom. In  $\alpha$  anomers, the exocyclic group at the anomeric center is *trans* to the exocyclic group at the anomeric reference atom or in opposite absolute configuration. In  $\beta$  anomers, the groups are *cis* to each other or in same absolute configuration.

In pyranoses in chair conformation, the anomers can also be described in terms of axial or equatorial. In Figure 2, the  $\beta$  anomer of the monosaccharide is shown. The anomers can interconvert which is called mutarotation or anomerization. On the one hand, the equatorial position in chair conformation is preferred over the axial position due to steric interaction as in 1,3-*syn*-diaxial interactions. On the other hand, the anomeric effect describes a tendency of heteroatomic substituents adjacent to the heteroatom in the ring to prefer an axial position. This effect is not completely understood but can be explained by negative hyperconjugation between a lone pair of the heteroatom in the ring and the  $\sigma^*$  orbital of the heteroatom in axial position.

A biologically important monosaccharide is fucose which is shown in several chemical representations in Figure 2. Fucose, a 6-deoxy-L-galactose is easily distinguishable from many other hexoses arising from the lack of the hydroxyl group at C-6 position and the L-configuration, rarely occurring in mammalian cells. Further important deoxy saccharides are deoxyribose, a 2-deoxy-D-ribose, which is name-giving for deoxyribonucleic acids (DNA) and rhamnose, a 6-deoxy-L-mannose.

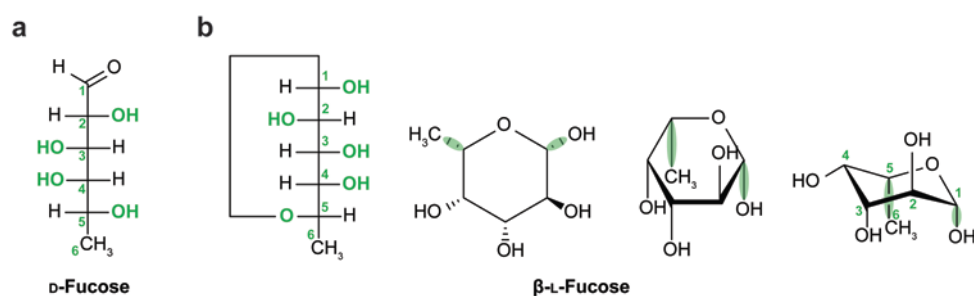


Figure 2: Different representations of fucose. From left to right: synthetic D-fucose in open chain form, naturally occurring  $\beta$ -L-fucose in pentose form in Fischer representation, in a simple skeletal structural formula, in Haworth projection and in chair conformation. Selective green highlighting shows the orientation of the hydroxyl groups in the isomers, the carbon numeration and the relative orientation of the anomeric atom and the anomeric reference atom defining the  $\beta$  anomer.

Going further to oligosaccharides, the complexity in saccharide chains is mainly governed by the monosaccharide composition, their connectivity and the configuration of the single monosaccharides. Additionally, glycans are not only composed of linear chains, but can also feature branched structures. The glycosidic linkage or connectivity is indicated with  $(1 \rightarrow x)$  with  $x = 2, 3, 4, 6$  where the first number refers to the anomeric carbon at C-1 at one monosaccharide and the second number to the position in the ring at the other monosaccharide.

The representation of molecules with chemical formulas is very challenging, which is caused by the immense structural complexity of glycans. Although chemical formulas are most precise and established, scientists have been using standardized nomenclatures since the 1980s.<sup>[32]</sup> The today most established symbol nomenclature for glycans (SNFG)<sup>[1]</sup> is explained briefly in Figure 3 and used throughout this thesis.

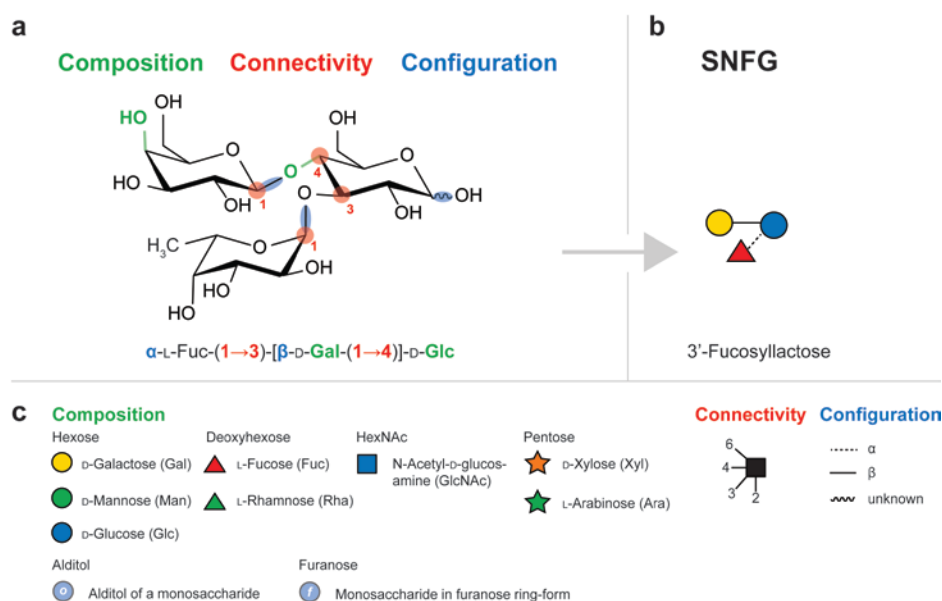


Figure 3: Symbol nomenclature for glycans (SNFG) which is used throughout this thesis.<sup>[1]</sup> Selected Monosaccharides (including the D- or L-form) are encoded with symbols of defined color and shape. Alditols of monosaccharides are indicated with an italicized "o" inside the respective symbol and furanoses with an italicized "f" inside the respective symbol. The connectivity or regiochemistry in a glycosidic bond is depicted by the bond angle. All linkages are assumed to originate from C-1 (exceptions possible). The configuration or stereochemistry at the anomeric center is defined by the type of the line.

Glycans are almost exclusively depicted as chair conformations, which is a basic simplification. There are 36 unique ring conformations, called ring puckers, grouped into five families: chair, half-chair, envelope, boat and skew boat conformation of which several subforms exist. Further conformational degrees of freedom are rotatable single glycosidic bonds and rotatable bonds of exocyclic groups. In the gas phase, the relative stability of the resulting conformation is mainly driven by electrostatics, e.g. midrange electron correlations (e.g. the anomeric effect) or the impact of hydrogen bonding networks in compact conformations.<sup>[33-35]</sup>

## 2.2 ROLE OF FUCOSYLATED GLYCANS

Fucose is a ubiquitous, deoxy monosaccharide building block which is present in a wide variety of organisms. It is common in glycopeptides, in *N*- or *O*-glycans and also in glycolipids. In mammalian carbohydrates, fucose is the fifth most abundant monosaccharide (7.2%) and even the second most abundant terminal monosaccharide unit (23.8%).<sup>[36]</sup> Among human milk oligosaccharides (HMO), up to 80% are fucosylated, depending on the individual's blood group status.<sup>[37]</sup> Fucosylated glycoproteins are usually produced in the Golgi apparatus and in the endoplasmic reticulum, during the final step of glycan processing by 13 so far identified fucosyltransferases.<sup>[38]</sup>

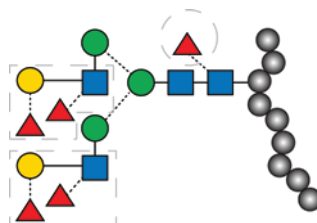


Figure 4: Example of a highly fucosylated glycoprotein found in parotid gland tissue (black shaded circles represent an arbitrary peptide chain).<sup>[39]</sup> The biantennary glycan consists of four terminal fucose units (dashed grey line, square) and one core fucose unit (dashed grey line, circle). The terminal fucose units are part of a prominent tetrasaccharide motive, the Lewis y antigen.

It is widely recognized that fucosylated glycans play critical biological roles, including in blood transfusion reactions or selectin mediated leukocyte-endothelial adhesion.<sup>[40]</sup> Alternating fucosylation is known to have a special impact in human diseases such as cancer. The fucosylated Lewis y ( $Le^y$ ) antigen is, for example, highly expressed on a wide range of tumors and by suppressing the expression, tumor growth can be inhibited.<sup>[6, 41-42]</sup> Many aspects still remain uncovered.



## 2.3 INVESTIGATED GLYCANS

The investigated glycans are naturally occurring in both mammalian and plant sources. The mammalian glycans are differently fucosylated and the plant glycans are decorated with arabinoses, an aldopentose monosaccharide in L-configuration.

The mammalian glycans studied here are found in two different blood group systems, the Lewis system (Le) and the ABO blood group system (H antigen, BG-H), as well as in human milk oligosaccharides (HMO). The blood group antigens Le<sup>y</sup> and Le<sup>b</sup> tetrasaccharides are constitutional isomers and have two fucose units at different non-reducing, terminal ends of their branched carbohydrate structure. They differ in the core disaccharide: galactose (Gal) is  $\beta$ -(1 $\rightarrow$ 4)-linked to N-acetylglucosamine (GlcNAc) in Le<sup>y</sup> whereas Gal is  $\beta$ -(1 $\rightarrow$ 3)-linked to GlcNAc in Le<sup>b</sup>. Structural subsets of Le<sup>y</sup> (Le<sup>y</sup>-series) with loss of one fucose monosaccharide (Le<sup>y</sup>-Fuc) as Y-type fragment ion<sup>[43]</sup> are the regioisomeric Le<sup>x</sup> and BG-H2 trisaccharides. Structural subsets of Le<sup>b</sup> (Le<sup>b</sup>-series; Le<sup>b</sup>-Fuc, Y-type fragment ion) are Le<sup>a</sup> and BG-H1. The anomeric center in these glycans is not defined and can adopt an  $\alpha$  and/or  $\beta$  configuration. Further, two alditols (ending -ol) synthetically derived from the trisaccharides Le<sup>x</sup> and BG-H2 are part of this work. With the loss of the stereogenic center at the GlcNAc, one configuration is present only. The selected HMOs are similar to Le<sup>x</sup> and BG-H2 carrying glucose (Glc) instead of GlcNAc units. These are 2'-fucosyllactose (2'-FL) and 3'-fucosyllactose (3'-FL).

The investigated plant sugars, on the other hand, consist of linear  $\beta$ -(1 $\rightarrow$ 4)-linked xylose (Xyl, X) chains with  $\alpha$ -(1 $\rightarrow$ 2)- or  $\alpha$ -(1 $\rightarrow$ 3)-linked L-arabinofuranose (Ara) either at the terminal monosaccharide or within the chain ( $\alpha$ -Ara-(1 $\rightarrow$ 2)-Xyl: A2,  $\alpha$ -Ara-(1 $\rightarrow$ 3)-Xyl: A3). They are building blocks in the chemical synthesis of larger plant sugars. Arabinoxylans are found in the cell walls where they serve a structural

role.<sup>[44-45]</sup> The plant sugars are equipped with an 5-aminopentanol linker (L) at the reducing end.

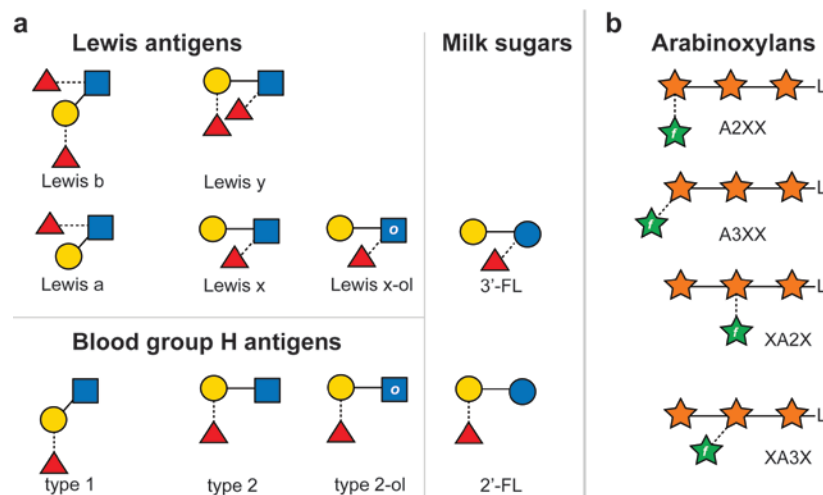


Figure 5: Investigated tri- and tetrasaccharides: a) The Lewis antigens and the blood group H antigens as well as the milk sugar are found in mammals. b) Arabinoxylan chains are plant sugars that feature characteristic repeating patterns of tetrasaccharides. The sugars carry a linker (L) at the reducing end.

## 2.4 FUCOSE MIGRATION IN MASS SPECTROMETRY — STATUS QUO

A reoccurring challenge in mass spectrometry of fucosylated glycans is fucose migration.<sup>[46-54]</sup> This intramolecular rearrangement reaction can lead to erroneous sequence assignments. During migration, a fucose unit is typically transferred from the non-reducing end of a glycan chain to adjacent or remote monosaccharides. The phenomenon has exclusively been observed in fragmentation experiments with collision-induced dissociation (CID). In fragmentation experiments, fucose migration is accompanied by an internal residue loss (IRL). An unexpected mass-to-charge ratio indirectly indicates the occurrence of the reaction. IRL, unlike the production of internal fragments, always includes bond cleavages and a subsequent internal bond formation. The terms IRL, fucose migration or also hexose migration

are used interchangeably in literature, because the observed fucose or hexose migrations always include IRL.

Rearrangement reactions in mass spectrometry can provide valuable information on the 3-dimensional structure of molecules in the gas phase, but also provide “relatively unpredictable possibilities of molecular rearrangement” as McLafferty<sup>[55]</sup> strikingly stated in 1959. The McLafferty rearrangement, a cyclic rearrangement of radical cations and unsaturated functional groups, is today one of the best studied rearrangement reactions occurring during the fragmentation of metastable species. As initially stated, another well-studied rearrangement reaction is peptide scrambling. Here, the rearrangement of a peptide sequence *via* a transient macrocyclic intermediate formed during CID can lead to false sequence assignments.<sup>[14, 19, 26]</sup>

In 1983, McNeil first reported an internal monosaccharide loss with migration to the alditol residue of per-*O*-alkylated oligosaccharide alditols during chemical ionization mass spectrometry.<sup>[28]</sup> By varying the *O*-ethylation position in *O*-methylated oligosaccharide alditols, McNeil was able to determine the monosaccharide in the chain that is migrating. Since then, a few mechanistic approaches for IRL have been proposed.<sup>[48-53]</sup> The reaction has been observed for protonated and doubly protonated ions as well as for ammonium adducts. The necessity of mobile protons or at least poor charge fixation is pointed out in almost all publications, suggesting that the reaction is charge-induced. The free hydroxyl groups within the oligosaccharides can display a hydrogen bonding network of vicinal and *syn*-diaxial hydrogen bonds in which proton or charge transfer is likely to be found. This promotes a highly dynamic ion structure. Charge-remote reactions have been discussed in molecules with functional groups of high proton affinity.

Nevertheless, this explanation lacks plausibility, because the reaction is not observable in sodium adduct ions as well as in deprotonated ions.<sup>[54]</sup> Both short- and long-range migration reactions are possible. For both cases, the close proximity in space of the migrating residue and the destination within the chain is most likely prerequisite to the reaction and at the same time difficult to predict, especially for long-range migration reactions. Therefore, the main difference in the mechanisms is the destination of the migrating monosaccharide.

Regarding the time scale of the reaction, it has been shown that species analyzed in an ion trap (millisecond range) and by matrix-assisted laser desorption ionization-TOF/TOF-MS (microsecond range) showed similar rearrangement patterns.<sup>[46]</sup> Therefore, the reaction can be faster than microseconds. Regarding the energy barrier of the reaction, the abundance of ion signals resulting from IRL is collision energy-dependent. Interestingly, when plotting the relative abundance of an ion against the collision energy, the ion from a simple loss of a terminal fucose and the ion from IRL with migration of fucose show the same curve shape indicating similar mechanisms.<sup>[49]</sup>

The exact mechanism of fucose migration remains unsolved to date. As one of the first, Brüll, *et al.*<sup>[53]</sup> suggested that the hydroxyl group at C-6 position attacks the anomeric center of the migrating group, a new (1→6)-glycosidic bond forms and an internal residue cleaves. In the investigations, it was shown that the reaction is independent of anomericity and linkage-type. Kováčik, *et al.*<sup>[52]</sup> formerly proposed that (1→2) linkages are a prerequisite to IRL. Since then, IRL has been observed for (1→2)-, (1→3)-, (1→4)- and (1→6)-linked migrating residues. Later, Ernst, *et al.*<sup>[51]</sup> proposed that the oxygen of the amide group of a sialic acid attacks the anomeric center of fucose and a new bond forms, leading to an imine group with the proton

located at the reducing end of the chain. Interestingly, the internal residue loss is then a reaction subsequent to the migration.

Later, Ma, *et al.*<sup>[48]</sup> suggested a detailed mechanism in which a ring oxygen atom is protonated with subsequent cleavage of the adjacent C-1–O bond, resulting in a carbenium ion at the anomeric center of the migrating group. In 6-deoxy monosaccharides, the ring oxygen has a slightly higher proton affinity than in other monosaccharides. Therefore, a transfer of the mobile proton from the linker is not unlikely. Then, the oxygen of the flavonoide residue linked to the reducing end of the diglycoside attacks the carbenium ion at the anomeric center and a semirigid internal residue is eliminated from the oligosaccharide. The migrating residue is rhamnose, a 6-deoxy-L-mannose. As Harvey, *et al.*<sup>[49]</sup> show, any glycosidic bond oxygen in the oligosaccharide can serve as attacking group in this mechanism. In the publication, it is suggested that in oligosaccharides with 2-aminobenzamide linker an attack from the nitrogen in the linker with a transfer of the migrating residue and a subsequent glycosidic bond cleavage of the terminal residue is more plausible than an elimination of a semirigid internal residue. The mechanism combines a migration reaction, which is independent of an internal loss with a subsequent fragmentation, as already suggested for sialic acids.

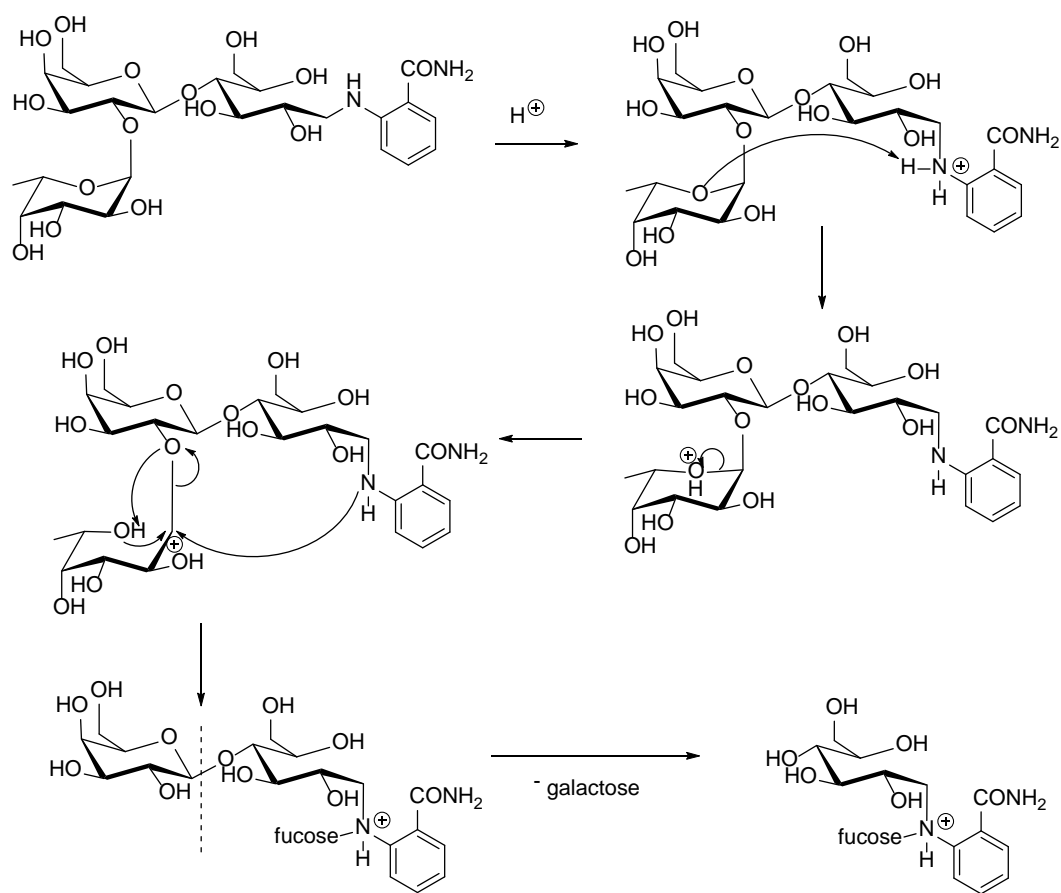


Figure 6: Mechanism for IRL during fragmentation of 2-aminobenzamide-derivatized 2'-FL (redrawn from Harvey, *et al.*<sup>[49]</sup>). First the fucose unit migrates to the linker and then the terminal glycosidic bond is cleaved.

A similar reaction pathway is suggested by Franz and Lebrilla<sup>[50]</sup> with the difference that the destination of migration is a remote hydroxyl group within the oligosaccharide. It can be ruled out that the amine linker is the only destination of migration, because IRL is observed in oligosaccharides with methylated amine linker.

In a recent publication by Hecht, *et al.*<sup>[56]</sup>, an IRL with migration of xylose is reported. Xylose, unlike rhamnose and fucose, is not a 6-deoxy monosaccharide, but

an aldopentose. Further migration reactions with IRL have been observed for mannose<sup>[47]</sup> and glucuronic acid<sup>[52]</sup>. It is found that up to five mannose residues can migrate in labelled oligomannose *N*-glycans from Ribonuclease B.

A very effective way to prevent IRL, fucose migration or hexose migration in tandem mass spectrometry experiments is measuring metal adducts or deprotonated ions. Furthermore, procainamide labeling<sup>[57]</sup> and the use of free radicals<sup>[58]</sup> suppress the reaction. Permethylation and peracetylation on the other hand do not in all cases prevent the reaction.<sup>[28, 50, 53]</sup>

Table 1: Selected literature on glycan rearrangement. In all publications, tandem mass spectrometry was employed.

Glycan or Glycoconjugate	Observation	Investigated Ions	Reference
<ul style="list-style-type: none"> <li>Trisaccharides, underivatized and per-<i>O</i>-methylated, with only (1→6)-linked residues and one or two 3-deoxy-Gal, 3-deoxy-3-fluoro-Gal or 6-deoxy-6-fluoro-Glc</li> </ul>	Internal loss with migration of deoxy-fluoro or <b>deoxy residues</b>	[M+H] <sup>+</sup>	Brüll, <i>et al.</i> <sup>[53]</sup>
<ul style="list-style-type: none"> <li>Tri- and tetrasaccharides, underivatized and per-<i>O</i>-methylated, containing differently attached Glc, GalNAc and Rha</li> </ul>	Internal loss with migration of <b>Rha</b> or glucuronic acid	[M+H] <sup>+</sup> , [M+Na] <sup>+</sup> , [M-H] <sup>-</sup>	Brüll, <i>et al.</i> <sup>[54]</sup>
<ul style="list-style-type: none"> <li>Sialyl-Le<sup>a</sup> and sialyl-Le<sup>x</sup></li> </ul>	Internal loss with migration of <b>Fuc</b>	[M+H] <sup>+</sup> , [M+NH <sub>4</sub> ] <sup>+</sup>	Ernst, <i>et al.</i> <sup>[51]</sup>
<ul style="list-style-type: none"> <li>LNFP I and LNDFH I, all labelled</li> </ul>	Internal loss with long-range migration of <b>Fuc</b>	[M+H] <sup>+</sup> , [M+Na] <sup>+</sup>	Franz and Lebrilla <sup>[50]</sup>
<ul style="list-style-type: none"> <li>2'-FL, LNT, LNFPI, LNFPII, LNFPIII, LNDFHI, Le<sup>a</sup>, Le<sup>x</sup>, all labelled</li> </ul>	Internal loss with migration of <b>Fuc</b>	[M+H] <sup>+</sup> , [M+Na] <sup>+</sup> [M+2H] <sup>2+</sup>	Harvey, <i>et al.</i> <sup>[49]</sup>
<ul style="list-style-type: none"> <li>Hexasaccharide containing Xyl, Man, GlcNAc</li> </ul>	Internal loss with migration of Xyl	[M+H] <sup>+</sup>	Hecht, <i>et al.</i> <sup>[56]</sup>
<ul style="list-style-type: none"> <li>Natural occurring oligosaccharides</li> </ul>	Internal loss with migration of <b>Rha</b>	[M+H] <sup>+</sup> , [M+Na] <sup>+</sup>	Kováčik, <i>et al.</i> <sup>[52]</sup>
<ul style="list-style-type: none"> <li>Flavonoid <i>O</i>-diglycosides</li> </ul>	Internal loss with migration of <b>Rha</b>	[M+H] <sup>+</sup>	Ma, <i>et al.</i> <sup>[48]</sup>
<ul style="list-style-type: none"> <li>Biantennary <i>N</i>-glycans with Le<sup>x</sup> and/or LacdiNAc, native and labelled</li> </ul>	Internal loss with migration of <b>Fuc</b> between antennae	[M+2H] <sup>2+</sup> , [M+H+Na] <sup>2+</sup> , [M+H+NH <sub>4</sub> ] <sup>2+</sup>	Wuhrer, <i>et al.</i> <sup>[46]</sup>
<ul style="list-style-type: none"> <li>Oligomannose <i>N</i>-glycans from Ribonuclease B, all labelled</li> </ul>	Internal loss with migration of up to five Man	[M+H] <sup>+</sup> , [M+Na] <sup>+</sup>	Wuhrer, <i>et al.</i> <sup>[47]</sup>



## 2.5 INFRARED SPECTROSCOPY OF GLYCANS IN THE GAS PHASE

Infrared (IR) spectroscopy or vibrational spectroscopy investigates the interaction of IR light with molecules. IR light expands from the edge of the visible spectrum at 780 nm to 1 mm wavelength and can be further divided into the higher energy, near IR ( $< 3\ \mu\text{m}$  or  $> 4000\ \text{cm}^{-1}$  wavenumbers), mid IR ( $3\text{--}50\ \mu\text{m}$  or  $4000\text{--}400\ \text{cm}^{-1}$ ) and lower energy, far IR ( $> 50\ \mu\text{m}$  or  $400\text{--}10\ \text{cm}^{-1}$ ) regime. The mid-IR regime is typically used for chemical structure determination.

Molecules are non-rigid and can move in space by rotation, translation, and vibration resulting in  $3N$  degrees of freedom for  $N$  number of atoms. Each vibration of a molecule is called vibrational mode and a non-linear molecule has  $3N-6$  vibrational degrees of freedom ( $3N-5$  for linear molecules). If a molecule is exposed to IR light that is in resonance with a vibrational mode, the absorption of a photon can excite the molecule to a higher vibrational energy state. The distance of the two states equals the energy of the absorbed IR light. Vibrational modes with a periodic change of the dipole moment in the molecule are called IR active. IR inactive vibrational modes are for example stretching vibrations in symmetrical bonds. In general, bonds with stronger polarity and larger dipole moments have stronger IR absorptions.

The basic approximation to describe the force of a molecular bond is the helical spring with Hooke's law: the force required to extend a spring is proportional to the extension or distance with a given stiffness. In this approximation, the quantum mechanical description of vibrations in molecules is the harmonic oscillator with equidistant energy levels. Real molecular bonds, however, have an intrinsic anharmonicity. The harmonic oscillator fails to describe the repulsion of atoms at short distance and also the dissociation limit at large interatomic distance.

Furthermore, the energy levels are not equally spaced and the vibrational modes are not independent. A more elaborate description of the anharmonic nature of molecular bonds can be found in the Morse potential.

Most IR spectroscopy techniques are based on absorption spectroscopy, which measures the attenuation of light after its interaction with a solid, liquid, or gaseous sample. The Lambert-Beer law relates the wavelength dependent absorption of light to the absorption cross section and concentration of the attenuating species and the path length of the light through the sample. The light is measured in its initial intensity and after it passed through the sample. A prerequisite to this technique is a relatively high sample concentration which is given in liquid or solid samples. For gaseous samples, e.g. in ion traps, the difference between the initial light intensity and the intensity after passing through the low density sample is usually so small that it is not measureable.<sup>[59]</sup> Therefore, vibrational spectra in the gas phase are typically measured by means of action spectroscopy.

Action spectroscopy studies the effect that radiation has on a sample or the action it evokes, e.g. fragmentation or ionization yield. The fraction of molecules  $N_v$  affected can be expressed as

$$N_v = N_0 e^{-\sigma_v \Phi_v} \quad (1)$$

in which  $\sigma_v$  is the absorption cross section of the light attenuating molecule,  $\Phi_v$  the photon flux and  $N_0$  the initial number of molecules. In order to measure the fragmentation of a molecule, the investigated system has to have a low dissociation energy barrier or the light source has to be powerful enough to induce the absorption of multiple photons by a single ion. Two common setups are messenger (-tagging) spectroscopy and infrared multiphoton dissociation (IRMPD) spectroscopy. Typical light sources in these setups are high pulse energy optical

parametric oscillators or free-electron lasers (FEL). In IRMPD spectroscopy, the fragmentation of the investigated molecules is measured by the sequential absorption of multiple resonant photons. The energy from each absorbed photon is dissipated *via* intramolecular vibrational redistribution over the entire molecule and the molecule can be repeatedly excited from the ground state. This iterative process continues until the internal energy of the system exceeds the dissociation threshold. A drawback from this technique is that absorption bands are typically broadened and red-shifted and the relative intensities can also be affected.<sup>[59]</sup>

Messenger spectroscopy has been widely used since the mid 1980's and investigates the detachment of a weakly bound messenger tag upon absorption of a single or a very low number of photons. Lee and co-workers<sup>[60]</sup> first reported that small molecular ions or clusters can form weakly bound clusters with hydrogen atoms. The mass-to-charge-selected clusters, stored in an ion trap, were interrogated with a tunable IR laser and the hydrogen detachment was recorded with a significant mass shift. Typical messenger tags are rare gas atoms which have only weak interactions with the investigated ions and no intrinsic IR absorption. The rare gas atoms are typically bound to the molecules of interest by supersonic expansions. A most recent publication involves messenger spectroscopy with hydrogen and also nitrogen tags in a cryogenic ion trap combined with ion mobility-mass spectrometry separation to investigate carbohydrates.<sup>[61-64]</sup> Cryogenic cooling enables a rather soft attachment of more weakly bound messenger tags in the ion trap by buffer gas cooling with the messenger tags. Further, it enables a higher conformer selectivity which is especially important for conformationally flexible carbohydrates.

Another elaborate technique is cold-ion IR spectroscopy in helium nano-droplets. Ions are embedded in superfluid helium droplets of an average size of  $10^3$ – $10^5$

helium atoms at 0.4 K. The helium droplets are optically transparent within the IR range and show only weak interactions with the embedded molecular ions. They therefore provide an ideal cryogenic non-interacting environment. Upon absorption of IR light, the molecule in the droplet is excited, energy is transferred to the helium bath, helium evaporates from the droplet and the molecule is rapidly cooled again. After several iterations of photon absorption and evaporative cooling, the intact ion is ejected from the droplet and finally detected. The ion ejection mechanism is still under investigation. So far, it has been shown by theoretical calculations and comparison to ultraviolet-IR experiments that the absorption bands are not matrix-shifted.<sup>[65]</sup> The method was first shown for an SF<sub>6</sub> molecule by Goyal, *et al.*<sup>[66]</sup> in 1992. Since then, different groups have used the method to investigate amino acids<sup>[67]</sup>, peptides<sup>[65]</sup>, proteins<sup>[68-69]</sup> and most recently carbohydrates<sup>[29]</sup>.

### 3 EXPERIMENTS

#### 3.1 COLD-ION INFRARED SPECTROSCOPY

Referring to the title of the thesis, the main method employed in this work is cold-ion IR spectroscopy. The experimental setup has been described in previous publications<sup>[29, 69-71]</sup> and is a combination of MS and IR action spectroscopy in superfluid helium nano-droplets. The mass spectrometer is attached to the *Fritz Haber Institute (Berlin)* free-electron laser (FEL)<sup>[72]</sup>. The laser provides tunable, narrow-bandwidth, coherent light in the mid-IR range with a high photon flux (number of photons *per second per unit area*). The setup is schematically described in Figure 7. Ions are selected by their mass-to-charge ratio ( $m/z$ ), trapped in the ion trap and then singly encapsulated and cooled in superfluid helium nano-droplets travelling through the trap. The IR spectra are recorded in the detection region of the instrument. There, the IR beam overlaps with the doped helium nano-droplets and the ion signal is recorded with a time-of-flight (TOF) mass analyzer. The IR spectrum is the ion signal as a function of the laser wavelength.

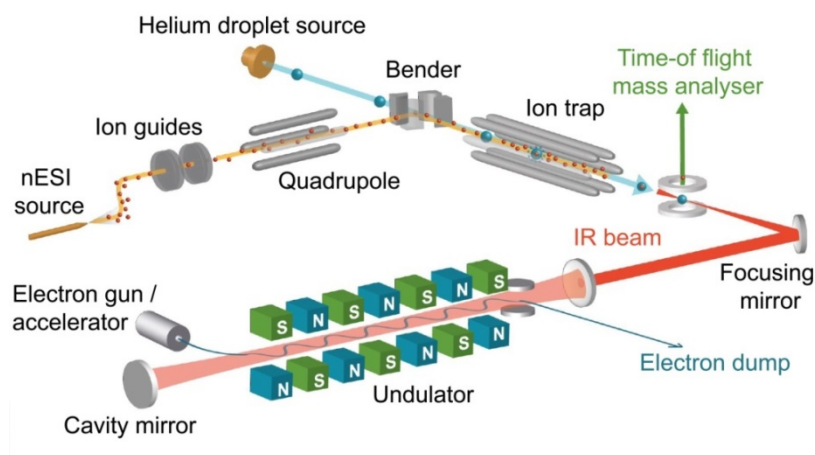


Figure 7: Schematic view of the experimental setup and the attached FEL.<sup>[69]</sup> The setup mainly consists of a nano-electrospray ionization source, a quadrupole mass

filter and a helium droplet source which is on-axis with a coolable ion trap and the IR laser beam.

The front end of the cold-ion IR spectroscopy instrument is a modified quadrupole TOF Ultima (*Waters Corporation*). The analyte is ionized with a nano-electrospray ionization (nESI) source. The nESI glass capillaries are produced with a micropipette puller (Model P-1000, *Sutter Instrument*) and Pd/Pt coated with a sputter coater (Sputter Coater HR 208, *Cressington*). The tip of the glass capillaries initially has a diameter of about 1–2  $\mu\text{m}$ . After fixed onto the needle holder, the capillaries are cut at the tip to a diameter of about 3  $\mu\text{m}$  with a wall thickness of less than 100 nm. The analyte solution is injected into the glass capillary and pushed to the tip of the capillary by applying an air flow. For the formation of charged droplets, a voltage of about 1 kV is applied. With the evaporation of solvent and fission of droplets by Coulomb repulsion, molecular ions form and are deflected towards the skimmer. The flight path of the ions at the inlet to the instrument is in Z-shape. The skimmer is in 90° angle to the glass capillary and the first of two, neighboring ring electrode ion guides in 90° angle to the skimmer. In the adjacent quadrupole mass filter the ions are selected by their mass-to-charge ratio. Finally, the ions are analyzed by their mass-to-charge ratio with the first TOF mass analyzer. The TOF mass analyzer is a reflectron analyzer which is usually operated in W mode with an ion mirror within the flight tube. The ions are detected using a micro channel plate.

The second flight path of the ions coming from the quadrupole is into the core of the mass spectrometer, the linear hexapole ion trap. The ions are deflected by 90° in the quadrupole beam deflector. The ion trap has a length of 30 cm and is coolable to about 80 K by directing gaseous nitrogen through a reservoir of liquid nitrogen into the copper housing of the trap. If not explicitly stated, the experiments in this work were performed with a non-cooled ion trap at room temperature. The incoming ions

have a kinetic energy of 34 eV, the DC bias of the trap is at 30 V and the endcap electrodes at the entrance and the exit are kept at 33 V. The longitudinal confinement of the ions is achieved by collisional-cooling with helium, a neutral buffer gas. Collisions of the ions with the buffer gas remove the excess of kinetic energy from the ions and enable trapping. The ion trap can either be emptied regularly or in case of a weak ion signal, ions can be accumulated throughout the measurement.

The helium nano-droplets or clusters with an average size of  $10^5$  helium atoms are generated by expanding high purity helium gas into vacuum from very low temperature and high pressure. The gas passes through a pulsed cryogenic Even-Lavie valve, which is operated at a repetition rate of 10 Hz with an opening time of 17  $\mu$ s, a stagnation pressure of  $6.8 \cdot 10^6$  Pa and a nozzle temperature of about 21 K. After a droplet beam is released into the vacuum chamber, the central part of the beam is cut out by a skimmer. The droplets have typical velocities of 400–500 m/s and a spatial spread of a few centimeters in the detection region of the instrument. The helium droplets pick up the ions from the trap and subsequently cool the encapsulated ions to the temperature of superfluid helium (0.4 K) by evaporative cooling. Multiple ion pick up is highly unlikely to occur because of the ion density in the trap, the geometry of the trap and the average size of the helium nano-droplets. The doped helium nano-droplets overcome the longitudinal trapping potential because of their large mass and high velocity.

Reaching the detection region of the instrument, the beam of doped nano-droplets overlaps with the IR laser beam. In case the wavelength of the laser is in resonance with a vibrational transition of a molecule, photons are absorbed, the molecule is excited and ejected from the helium nano-droplet. The ion ejection efficiency is

measured background-free in the attached second TOF, a home-built Wiley MacLaren type TOF mass spectrometer with an electron multiplier detector. The ion signal within a specific mass range is recorded as a function of the IR wavelength. In a scan, the exact IR wavelength and full width at half maximum (FWHM) are recorded with each set wavelength step and after 30 steps, the laser power is measured. The detectors are located at the FEL facility, outside the experimental setup described here. Crucial in the course of a scan of an IR wavelength regime is the setting of the trigger system, which consists of three delay generators.

The alignment of the laser with the helium nano-droplet beam is adjusted regularly to optimize the ion signal on the second TOF mass spectrometer. Therefore, a helium neon laser, which emits light in the visible spectrum, is operated instead of the FEL. The laser beam is focused into the instrument by movable, optical mirrors including a variable focusing mirror. With the latter, the laser beam is focused to the detection region.

With a high focus, a high photon flux is achieved during overlap of the droplet beam and the laser. In order to detect weak vibrations, a higher laser focus is used in the measurements of this work. Possible fragmentation of the molecule after or during ejection is also monitored for potential evaluation.

The absorption process, as described in chapter 2.5, is a non-linear process because of multiple photon absorption and the exact dependency between laser power and ion ejection efficiency is not fully understood. Therefore, ion signal intensities are a general guide, but the peak positions are strongly characteristic. The laser power, measured every 30 scan steps, to a specific wavelength is calculated as quartic polynomials. The ion signal is then simply divided by the laser power as a first order approximation. The ion signal intensity is then normalized to [0,1] in the



range of 1000–1200  $\text{cm}^{-1}$  with lower laser focus. The ion signal intensity in the range of 1200–1800  $\text{cm}^{-1}$  is normalized to a lower maximum, usually [0,0.7] to account for the higher laser focus. For each molecule, at least two scans are measured and averaged, provided the spectrum has a high reproducibility. An example for the high reproducibility of glycan spectra and the averaging of multiple curves is shown in Mucha, *et al.*<sup>[29]</sup>. For simplification, the higher wavenumber region is shown excluding the measured overlap, provided the higher laser focus only changes the intensity of the bands in the region of 1100–1200  $\text{cm}^{-1}$ . In case new bands appear with a higher focus, the overlap is shown. Regions with no absorption bands can be excluded from the representation indicated with breaks in the  $x$ -axis.

Glycan fragmentation is performed by in-source activation and subsequent mass selection. The mass spectra at two different source conditions (harsh *vs.* soft conditions) are attached in the appendix for one of the tri- and one of the tetrasaccharides. All measurements of intact ions are performed with soft conditions to minimize the extent of activation of the ions.

Selected technical data of the *Fritz Haber Institute (Berlin)* FEL is given in Table 2. The FWHM bandwidth of the laser is 0.5%. In this work the measured wavenumber regimes range from 1000–1800  $\text{cm}^{-1}$  which results in a laser bandwidth of 5–9  $\text{cm}^{-1}$ , respectively.

Table 2: Selected technical data of the *Fritz Haber Institute (Berlin)* FEL<sup>[72]</sup>.

Parameter	Unit	Regularly achieved
Electron energy	MeV	18–44
Wavelength regime	$\mu\text{m}$	4–50
FWHM bandwidth	%	0.5
Macro pulse energy	mJ	< 100
Macro pulse length	$\mu\text{s}$	1–15
Macro pulse repetition rate	Hz	$\leq 20$
Micro pulse length	ps	1–5
Micro pulse repetition rate	GHz	1

### 3.2 ION MOBILITY-MASS SPECTROMETRY

A second method used in this thesis is ion mobility-mass spectrometry (IM-MS). In the following paragraphs, a basic introduction to IM-MS with a brief description of the calculation of collision cross sections (CCS) as well as the experimental setups will be shown. The findings obtained by IM-MS experiments are valuable to strengthen the results of the spectroscopic work. Nevertheless, the fundamentals of IM-MS, as an elaborate separation technique, are, owing to the focus of the master thesis, only summarized within this chapter.

The combination of ion mobility spectrometry and mass spectrometry is a promising orthogonal technique in glycan analysis. In a typical IM-MS setup, ions travel through a gas-filled cell at ambient pressure or light vacuum under the influence of a weak electric field. The ions collide with the gas atoms or molecules of the buffer gas, which are typically helium, nitrogen or argon. The mobility of the ions in the drift cell is determined by their mass, size, shape and charge. Extended

molecules undergo more collisions with the buffer gas than more compact forms and therefore have a lower mobility. Ions carrying a higher charge have a higher mobility.

The drift time  $t$  is highly dependent on measurement conditions and instrumental parameters. However, the rotationally averaged CCS, which can be derived, is characteristic for each compound and independent of the instrument. The drift velocity  $v$  of an ion at constant pressure  $p$  and temperature  $T$  can be derived from the drift time and the length of the drift cell  $L$ . It is further proportional to the mobility constant  $K$  and the electric field  $E$  which is again defined by the drift voltage and the length of the drift cell.

$$v = \frac{L}{t} = K \cdot E = K \cdot \frac{V_D}{L} \quad (2)$$

The CCSs  $\Omega$  are determined using the Mason-Shamp equation

$$\Omega = \frac{ze}{16N} \frac{1}{K_0} \sqrt{\frac{2\pi}{\mu k_B T}} \quad (3)$$

where  $ze$  is the total charge of the ion,  $N$  the drift gas number density,  $K_0$  the pressure and temperature normalized mobility constant,  $\mu$  the reduced mass of the ion and the drift gas and  $k_B$  the Boltzmann constant.

The measured drift time  $t_D$  is the sum of the drift time in the drift cell and an offset  $t_0$  which is the time the ion needs from the drift cell to the detector. With equation 2, a linear regression is derived. In practice, the drift time is measured at different drift voltages and plotted as a function of  $\frac{1}{V_D}$ .

$$t_D = t + t_0 = \frac{L^2}{K} \frac{1}{V_D} + t_0 \quad (4)$$

The mobility constant is then part of the slope. With the mobility constant, the CCS can be calculated according to equation 3.

The experiments were performed on two different instruments; one is a modified drift-tube Synapt G2-Si quadrupole ion mobility time-of-flight mass spectrometer (*Waters Corporation*), the other is also a drift-tube quadrupole ion mobility time-of-flight mass spectrometer, but home-built. The main difference between the instruments and the reason for conducting experimental work on two different drift-tube instruments is the relative harshness of the two instruments and also the resolution.

The core of the commercially available instrument is modified to a radio-frequency confining drift cell instead of a travelling-wave mobility cell. In the front end region, the analyte is ionized in a nESI source, which is attached to a Z-shape inlet, similar to the previous setup. Subsequently, the ions pass through a stacked ring ion guide called StepWave (*Waters Corporation*), which removes remaining, neutral contaminants, and are then mass-to-charge-selected in a quadrupole. The core of the instrument is the so called TriWave (*Waters Corporation*), which consists of three stages: two collision cells before and after the ion mobility cell. An additional helium cell is inserted between the first collision cell and the ion mobility cell to facilitate the transfer of the ions between different pressure stages. The ions are analyzed by their mass-to-charge ratio in the reflectron TOF mass analyzer and then detected.

Selected instrument specifications and applied settings: drift gas used helium or nitrogen, length drift cell 25.05 cm, pressure in ion mobility cell 293 Pa (2.2 Torr), temperature in ion mobility cell 25–28 °C and typical drift voltage 75–350 V.

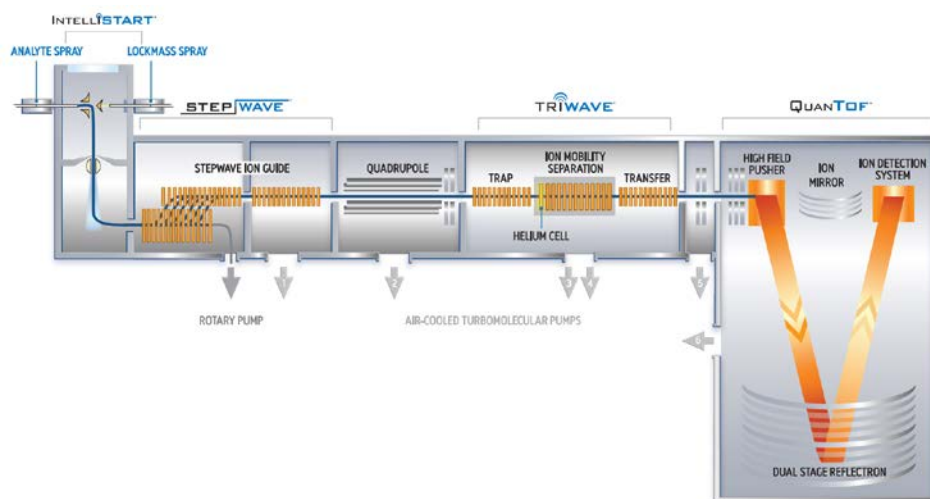


Figure 8: Schematic view of a Synapt G2-Si mass spectrometer (Waters Corporation): the instrument consists of a nESI source, a StepWave ion guide and a quadrupole mass filter, two collision cells before and after the ion mobility cell, an additional helium cell and a TOF mass analyzer with detector. Illustration provided by Waters Corporation.

The home-built drift-tube quadrupole ion mobility time-of-flight mass spectrometer is connected to the *Fritz Haber Institute (Berlin)* FEL. In IRMPD experiments, mass-to-charge- and mobility-selected ions are excited at room temperature within the interaction region of the instrument. It is possible to perform ion mobility experiments as part of an IRMPD experiment or as an independent measurement. In this work, the latter was explored. In the front end region of the instrument, ions are ionized with a nESI source and guided into the instrument in a linear fashion (on-axis). The drift tube is 80.55 cm long and framed by an entrance and an exit ion funnel. The drift time separated ions are then mass-to-charge-selected in a quadrupole mass filter, pass through the interaction region and are then analyzed and detected in a TOF mass spectrometer.

Selected instrument specifications and applied settings: drift gas used helium, length drift cell 80.55 cm, pressure in ion mobility cell 400–420 Pa, temperature in ion mobility cell 22–23 °C, injection voltage 30–200 V and typical drift voltage 950–1200 V.

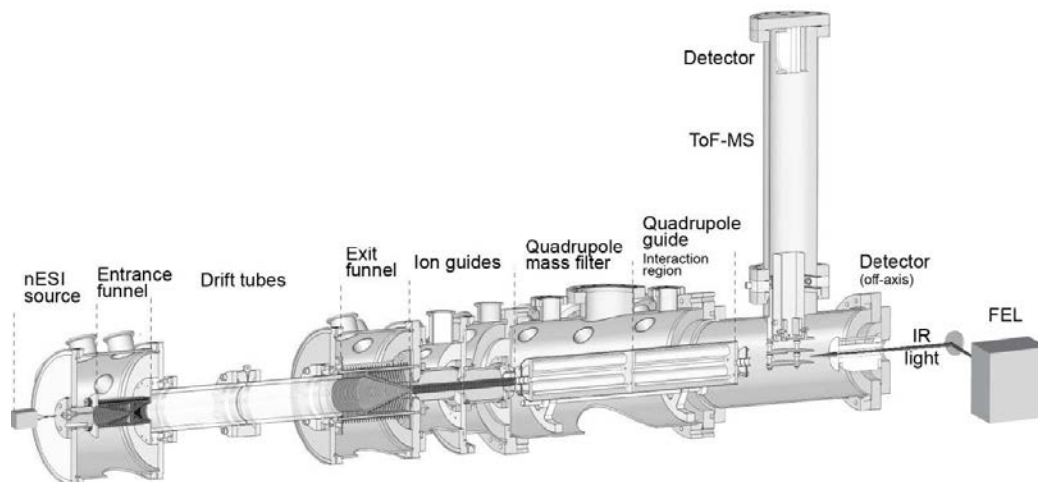


Figure 9: Schematic view of the home-built drift-tube mass spectrometer located at the *Fitz-Haber-Institute (Berlin)*. The ions are ionized in a nESI source, travel through the drift tube, are then mass-to-charge-selected in a quadrupole mass filter, analyzed in the TOF mass analyzer and detected. IRMPD experiments can be performed with the attached FEL (Illustration from Warnke, *et al.*<sup>[73]</sup>).

### 3.3 PREPARATION OF SAMPLES

The investigated oligosaccharides of the Lewis and ABO blood group system were purchased from *Biozol*. The human milk oligosaccharides were purchased from *Elicityl SA* and the plant sugars were kindly provided by the group of Dr. Fabian Pfrengle (*Max-Planck-Institut für Kolloid- und Grenzflächenforschung, Potsdam*). The oligosaccharides were used without prior purification and diluted in HPLC grade water to a concentration of 1 mM. The samples from the stock solutions were then further diluted in HPLC grade water/methanol (1/1, v/v) in concentrations of 20–

500  $\mu\text{M}$ . To promote the adduct formation in the measurements of  $[\text{M}+\text{NH}_4]^+$ ,  $[\text{M}+\text{NMe}_3\text{H}]^+$  and  $[\text{M}+\text{NEt}_3\text{H}]^+$ , ammonium acetate, trimethylammonium chloride and triethylammonium acetate, respectively, were added in concentrations of 1–5 mM. The reduced glycans of the Lewis and ABO blood group system were kindly provided by Christian Manz (*Freie Universität, Berlin*). For the corresponding protocol, please refer to Alexandra Stuckmann's (*Freie Universität, Berlin*) master thesis. The samples were used in concentrations of approximately 200  $\mu\text{M}$  diluted in HPLC grade water/methanol (1/1, v/v) with 0.1% formic acid.

The deuterated glycans in the hydrogen-deuterium in-source exchange experiment were obtained by applying a counter flow of nitrogen with  $\text{D}_2\text{O}$  at the source of the cold-ion IR spectroscopy instrument. The nitrogen flow was led through three reservoirs of fresh  $\text{D}_2\text{O}$  before reaching the source region.

## 4 FUCOSE MIGRATION — A UNIVERSAL PHENOMENON IN MASS SPECTROMETRY

Cold-ion infrared (IR) spectroscopy experiments were performed to study the chemical structure of fucosylated glycans in the gas phase and gain information on the functional groups in the molecule. Glycans with similar chemical structures were investigated with ion mobility-mass spectrometry (IM-MS) to determine their shape. Then, cold-ion IR spectroscopy was combined with a hydrogen-deuterium exchange experiment. To aid structural assignment, cold-ion IR spectra of precooled ions were measured and an in-source activation experiment in IM-MS was performed.

The investigated glycans (chapter 2.3) were selected by their structural relationship of the core di- or trisaccharide. The Lewis and ABO blood group antigens were investigated first. Then, further glycans with variations in functional groups or modifications of the reducing-end were chosen. Finally, a set of isomeric non-fucosylated glycans were studied.

### 4.1 COLD-ION INFRARED SPECTROSCOPY OF FUCOSYLATED GLYCAN IONS

Cold-ion IR spectra of the fucosylated glycan ions were obtained using the experimental setup and settings described in chapter 3.1.

To interpret the IR spectra of glycans, a general understanding of the typical absorption regions is useful. Typically, between 950 and 1200  $\text{cm}^{-1}$ , C–O stretching vibrations,  $\nu(\text{CO})$  of the hydroxyl groups in glycans are found. These transitions have a strong dipole moment and especially in larger glycans they dominate the spectrum. Between 1200 and 1500  $\text{cm}^{-1}$ , O–H bending modes,  $\delta(\text{OH})$  are present. In



saccharides containing an *N*-acetylhexosamine (HexNAc) unit, normal modes from the secondary amide group are observable.

#### 4.1.1 SODIUM ADDUCT IONS

To validate the use of the method for fucosylated glycans, IR spectra of sodiated fucosylated glycan ions were measured. For sodiated glycan ions, fucose migration reactions have been excluded in literature.<sup>[74]</sup> The IR spectra of the tetrasaccharides  $\text{Le}^y$  and  $\text{Le}^b$  as sodium adducts (both  $m/z$  698) are published in Mucha, *et al.*<sup>[29]</sup>. The IR spectra display a small number of well-resolved features, by which they can be discriminated unambiguously.

The IR spectra of the trisaccharides of the  $\text{Le}^y$ -series ( $\text{Le}^y$ -Fuc,  $\text{Le}^x$  and BG-H2) and of the  $\text{Le}^b$ -series ( $\text{Le}^b$ -Fuc,  $\text{Le}^a$  and BG-H1) measured as  $[\text{M}+\text{Na}]^+$  fragment and parent ions show unique IR fingerprint spectra and are given in Figure 11a and Figure 12a, respectively. The trisaccharides are  $m/z$  552. A schematic MS spectrum is given for both series in Figure 10.

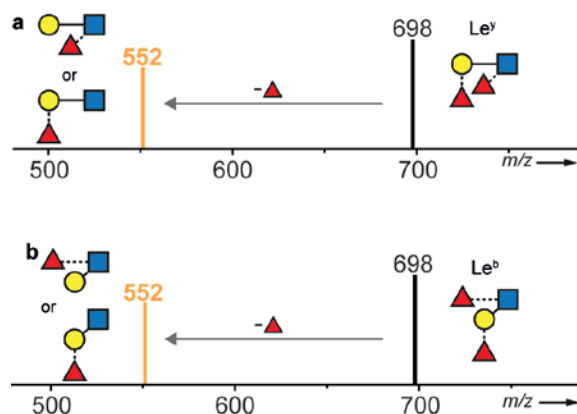


Figure 10: a) Schematic MS spectrum of  $\text{Le}^y$ :  $m/z$  698 is the  $[\text{Le}^y+\text{Na}]^+$  parent ion and  $m/z$  552 the possible isobaric  $[\text{Le}^y\text{-Fuc}+\text{Na}]^+$  fragment ions which are identical to  $\text{Le}^x$  and BG-H2. A complete mass spectrum is shown in the appendix. b) Schematic MS spectrum of  $\text{Le}^b$ :  $m/z$  698 is the  $[\text{Le}^b+\text{Na}]^+$  parent ion and  $m/z$  552

the possible isobaric  $[\text{Le}^b\text{-Fuc+Na}]^+$  fragment ions which are identical to  $\text{Le}^a$  and BG-H1.

The IR spectrum of  $\text{Le}^y\text{-Fuc}$  divides mainly into three parts within the range of 1000 to 1800  $\text{cm}^{-1}$ . Between 1020 and 1120  $\text{cm}^{-1}$  (C–O stretching region), four weaker absorptions and one characteristic split band with small shoulders to lower and higher wavenumbers are found. Around 1525  $\text{cm}^{-1}$ , three medium intensity features are present. At 1670  $\text{cm}^{-1}$ , one strong peak with two weak side peaks red- and blue-shifted are well-resolved. The peaks above 1500  $\text{cm}^{-1}$  are generally associated with vibrations of the secondary amide functional group.

To examine which of the two possible trisaccharides is present in the spectrum of  $\text{Le}^y\text{-Fuc}$ , the IR spectra of  $\text{Le}^x$  and BG-H2 were measured from standards. Both spectra contain features of the spectrum of  $\text{Le}^y\text{-Fuc}$  and share only a small number of features. Both spectra consist of the strongest absorption peak at 1670  $\text{cm}^{-1}$ , but only the spectrum of  $\text{Le}^x$  displays the blue-shifted and only the spectrum of BG-H2 displays the red-shifted weaker feature to the side of the main peak. The appearance of more than one well-resolved band around 1525  $\text{cm}^{-1}$  can indicate that more than one chemical structure and/or conformation is present. The spectrum of  $\text{Le}^x$  on the one hand yields one rather congested band and the spectrum of BG-H2 on the other hand shows three bands. In the C–O stretching region, the bands for the trisaccharide standards are slightly shifted to each other.

In summary,  $\text{Le}^x$  and BG-H2 have distinct spectra in which most likely more than one configuration ( $\alpha$  and/or  $\beta$ ) and/or lowest energy conformation is present. Fragmentation of the  $\text{Le}^y$  tetrasaccharide can lead to both trisaccharides. The spectrum of the fragmented tetrasaccharide exhibits features from both standard spectra which indicates that both chemical structures are present. The extent to

which each isomer is formed can be evaluated by linear combination analysis. Each spectral line is multiplied by a constant and the results are added to each other. The result is a third spectrum, the linear combination spectrum. The standard spectra are multiplied by 1 and added to each other. This linear combination is shown in Figure 11b (red stroke). The comparison of the linear combination to the spectrum of the fragmented tetrasaccharide shows that the spectral lines are almost identical. This indicates that both trisaccharides are about equally formed in the fragmentation of the tetrasaccharide.

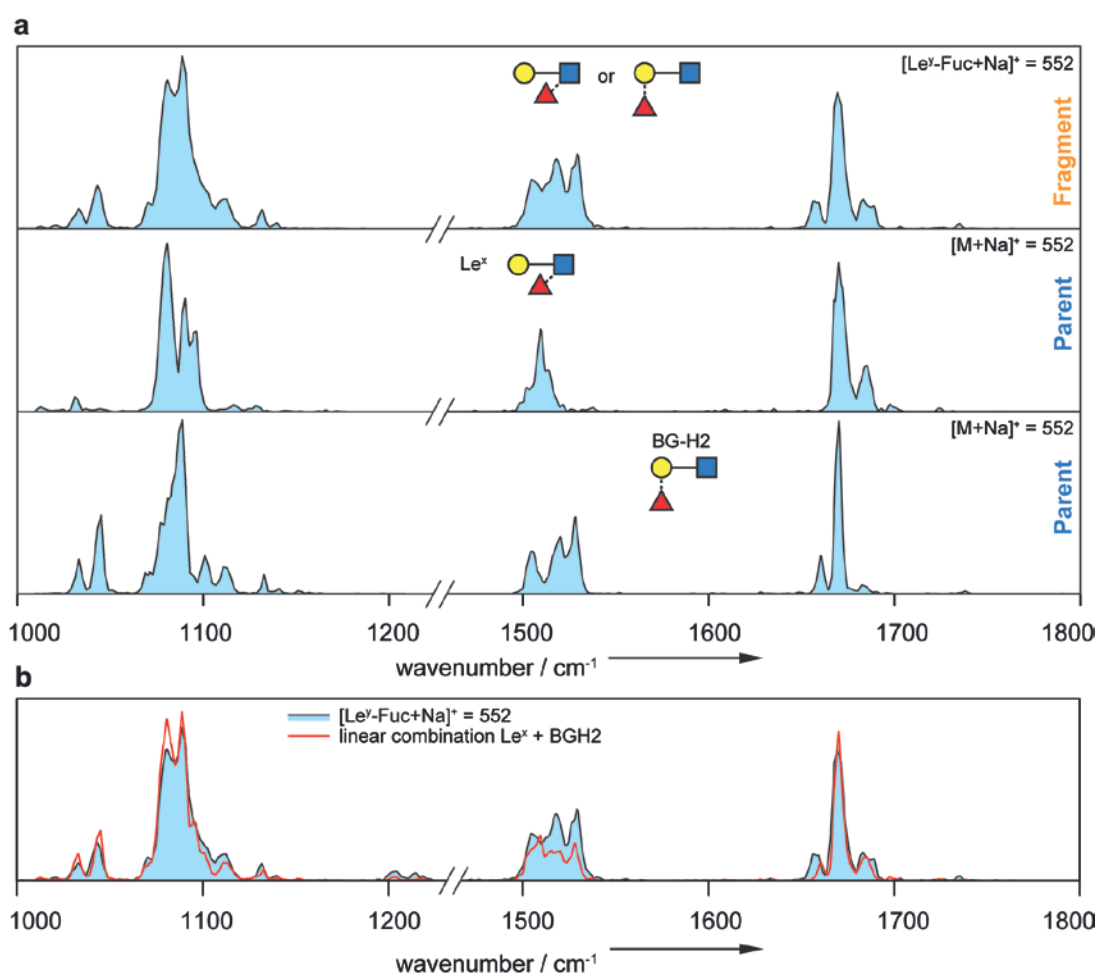


Figure 11: a) IR spectra of the fragment ion  $\text{Le}^y\text{-Fuc}$  (upper panel) and the parent ions  $\text{Le}^x$  (middle panel) and BG-H2 (lower panel) investigated as  $[\text{M}+\text{Na}]^+$  ions in the range of 1000-1800  $\text{cm}^{-1}$  (break between 1230 and 1470  $\text{cm}^{-1}$ ). The two spectra of the regioisomers  $\text{Le}^x$  and BG-H2 are distinguishable and the spectrum of  $[\text{Le}^y\text{-Fuc}+\text{Na}]^+$  shows characteristics of both of these. b) Overlay of the spectrum of  $[\text{Le}^y\text{-Fuc}+\text{Na}]^+$  (blue filled) and a linear combination (1/1) of  $\text{Le}^x$  and BG-H2 (red stroke).

The IR spectra of the  $\text{Le}^b$ -series measured as sodiated adduct ions are given in Figure 12a and are comparable to the spectra of the  $\text{Le}^y$ -series. The spectrum of  $\text{Le}^b\text{-Fuc}$  shows features of both standard trisaccharides ( $\text{Le}^a$  and BG-H1) and the

linear combination (1/1) of their spectra yields the spectrum of  $\text{Le}^b\text{-Fuc}$  (Figure 12b). In the fragmentation of the tetrasaccharide  $\text{Le}^b$ , both trisaccharides are about equally formed.

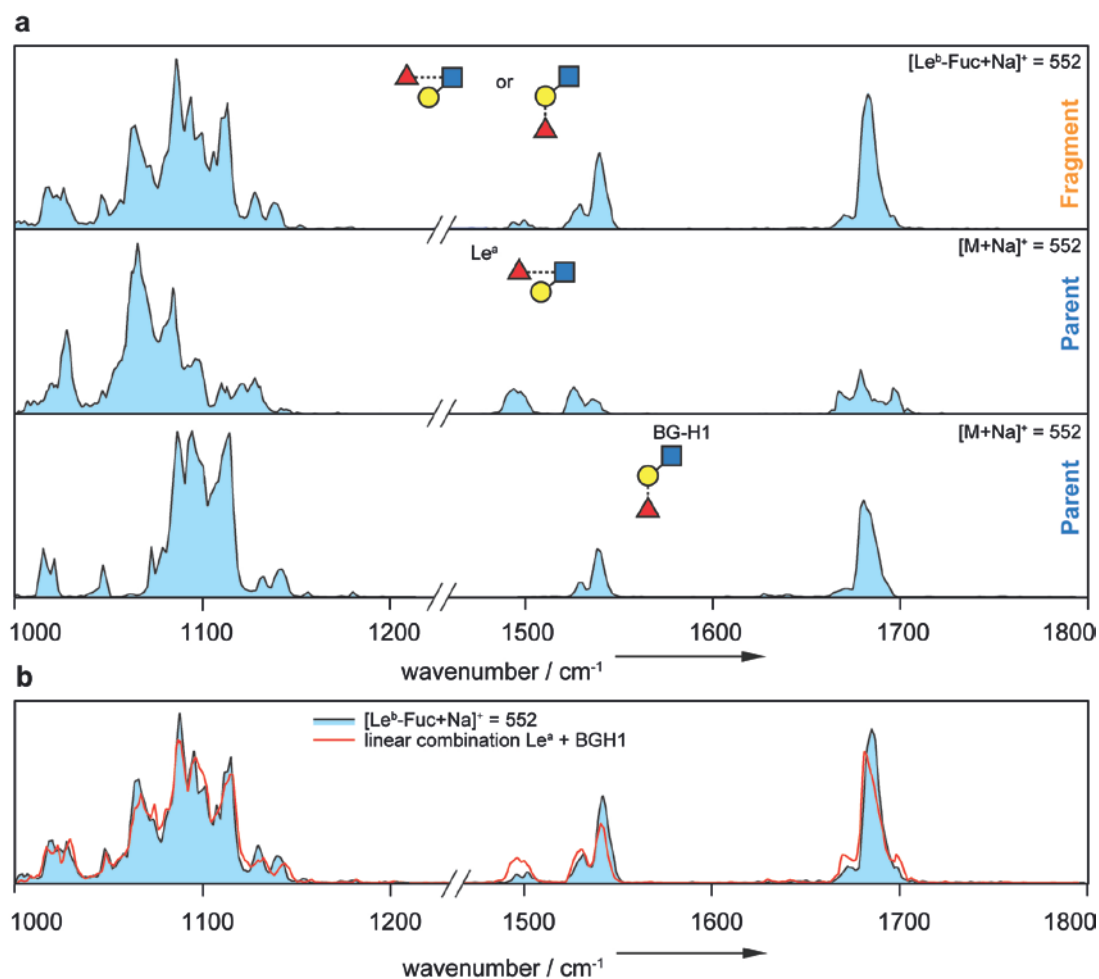


Figure 12: a) IR spectra of the fragment ion  $\text{Le}^b\text{-Fuc}$  (upper panel) and the parent ions  $\text{Le}^a$  (middle panel) and BG-H1 (lower panel) investigated as  $[\text{M+Na}]^+$  ions in the range of 1000-1800  $\text{cm}^{-1}$  (break between 1230 and 1470  $\text{cm}^{-1}$ ). The two spectra of the regioisomers  $\text{Le}^a$  and BG-H1 are distinguishable and the spectrum of  $[\text{Le}^b\text{-Fuc+Na}]^+$  shows characteristics of both of these. b) Overlay of the spectrum of  $[\text{Le}^b\text{-Fuc+Na}]^+$  (blue fill) and a linear combination (1/1) of  $\text{Le}^a$  and BG-H1 (red stroke).

#### 4.1.2 PROTONATED IONS

Fucose migration reactions are predominantly reported for protonated fucosylated glycan ions. To begin with, the IR spectra of the  $\text{Le}^y$ - and  $\text{Le}^b$ -series were measured as protonated fragment and parent trisaccharide ions equivalent to the investigation of the sodiated ions.

The IR spectra of the  $\text{Le}^y$ -series ( $\text{Le}^y\text{-Fuc}$ ,  $\text{Le}^x$  and BG-H2) measured as  $[\text{M}+\text{H}]^+$  fragment and parent ions exhibit a variety of individual bands (Figure 14a). On the contrary, the IR spectra of the  $\text{Le}^b$ -series ( $\text{Le}^a$  and BG-H1) measured as  $[\text{M}+\text{H}]^+$  parent ions do not show many distinct features (Figure 16). The trisaccharides of both series are  $m/z$  530. The fragmentation paths for both series are shown in the schematic MS spectrum in Figure 13.

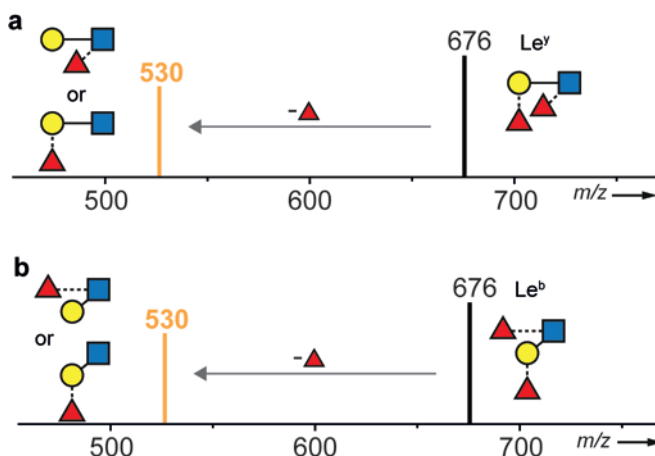


Figure 13: a) Schematic MS spectrum of  $\text{Le}^y$ :  $m/z$  676 is the  $[\text{Le}^y+\text{H}]^+$  parent ion and  $m/z$  530 the possible isobaric  $[\text{Le}^y\text{-Fuc}+\text{H}]^+$  fragment ions which are identical to  $\text{Le}^x$  and BG-H2. A complete mass spectrum is shown in the appendix. b) Schematic MS spectrum of  $\text{Le}^b$ :  $m/z$  676 is the  $[\text{Le}^b+\text{H}]^+$  parent ion and  $m/z$  530 the possible isobaric  $[\text{Le}^b\text{-Fuc}+\text{H}]^+$  fragment ions which are identical to  $\text{Le}^a$  and BG-H1.

In the first part of the IR spectrum from 1000 to 1200  $\text{cm}^{-1}$  of  $[\text{Le}^y\text{-Fuc+H}]^+$ , up to ten medium to high intensity features are resolved. From 1150 to 1640  $\text{cm}^{-1}$ , no absorptions are observed. In the last part of the spectrum around 1662  $\text{cm}^{-1}$ , one strong feature with high intensity is found. The FWHM of this rather broad band is 15  $\text{cm}^{-1}$  and therefore about twice the bandwidth of the laser (typical FWHM of  $\sim 0.5\%$  of the corresponding wavenumber).

The IR spectra of the intact standards  $\text{Le}^x$  and BG-H2 were measured and compared to the spectrum of  $\text{Le}^y\text{-Fuc}$ . The IR spectra of the two protonated standards and the IR spectrum of the fragmentation ions are almost identical. The peak positions match exactly. Small differences are a broad peak around 1140  $\text{cm}^{-1}$  in the spectrum of BG-H2 and a small peak at 1020  $\text{cm}^{-1}$  in the spectrum of  $\text{Le}^y\text{-Fuc}$ , both are missing in the two other spectra.

The identical IR spectra for the trisaccharide standards as well as the fragmented tetrasaccharide lead to the conclusion that the underlying gas-phase chemical structures are the same. The protonated  $\text{Le}^y$  fragment and possibly both protonated trisaccharide standards  $\text{Le}^x$  and BG-H2 undergo a rearrangement reaction — a fucose migration — to the same structure. This unknown structure can exist in multiple low-energy conformations. The intensities in the spectrum of the fragmented tetrasaccharide are partially quite different from the intact trisaccharides which can be associated with slightly varying low-energy conformational families or also a different ratio of reducing end configurations present. The occurrence of more than one conformation, nevertheless, has no impact on the interpretation of the data. The conclusion that  $\text{Le}^y\text{-Fuc}$ ,  $\text{Le}^x$  and BG-H2 yield the same gas-phase chemical structures is not affected by this. The probability that the spectra are coincidentally identical is negligibly small.

The chemical structure cannot be directly derived from the IR spectra. Possible reaction pathways are a rearrangement reaction to a third structure or an interconversion of one trisaccharide to the other. Generally, possible destinations for the fucose monosaccharide are any of the hydroxyl groups within the glycan or also the amide group at the GlcNAc. In literature, the migration of a fucose monosaccharide to an amide group of a sialic acid has been suggested.<sup>[51]</sup> Nevertheless, preliminary calculations by our group have shown that an iminium ion with a fucose monosaccharide at the oxygen atom of the amide is less stable in energy than glycans with fucose at one the hydroxyl groups. This can for example be explained by considering the stabilization of hydrogen bonding networks in glycans. These are disrupted for the resulting iminium ion.

Tandem MS spectra were recorded for the two protonated trisaccharides (see appendix). Products of a fucose migration with IRL are observable for BG-H2. The main migration product has a mass-to-charge ratio of a GlcNAc monosaccharide equipped with a fucose unit. For  $\text{Le}^x$ , migration products cannot be detected. This is not surprising because a migration product with unexpected mass-to-charge ratio would be a Gal monosaccharide equipped with a fucose unit. The proton is most likely located at the GlcNAc and the Gal-Fuc fragment would be neutral, therefore not detectable. The comparability of fucose migration in combination with IRL to fucose migration in intact ions is, however, limited because the ions exhibit different effective temperatures. As described in chapter 3.1, the measurements of the intact ions were performed with soft instrument settings to minimize the extent of activation.

To summarize, the first results show the occurrence of fucose migration in intact glycans ions. This is a novel observation. Further investigations in this thesis are,



therefore, focused on fucose migration reactions in intact glycans ions independent of a subsequent IRL and without extensive activation.

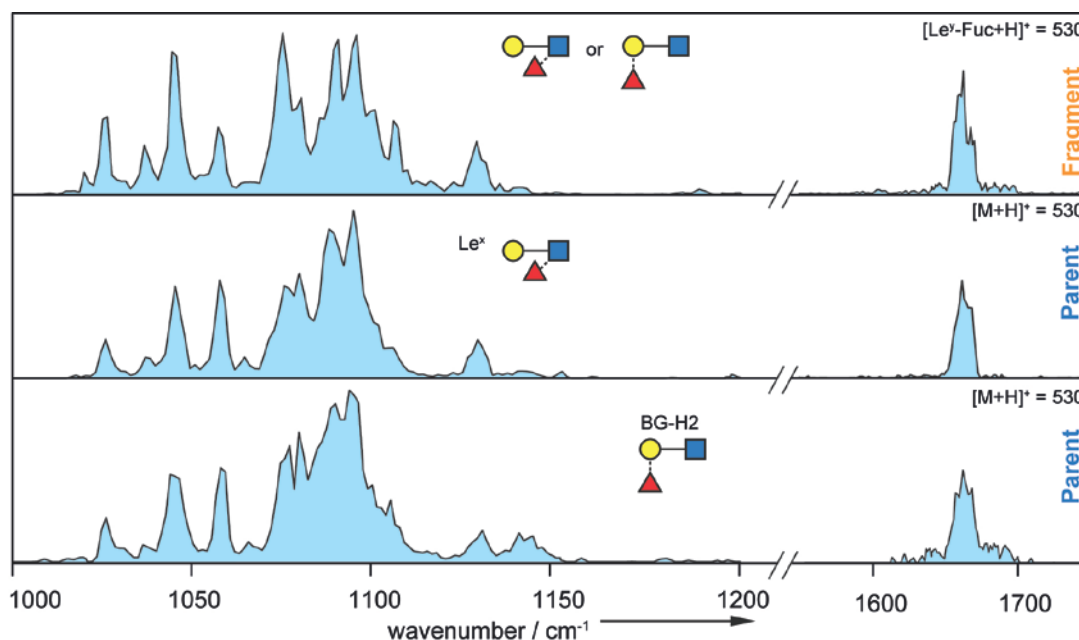


Figure 14: IR spectra of the fragment ion  $\text{Le}^y\text{-Fuc}$  (upper panel) and the parent ions  $\text{Le}^x$  (middle panel) and BG-H2 (lower panel) investigated as  $[\text{M}+\text{H}]^+$  species in the range of 1000-1730  $\text{cm}^{-1}$  (break between 1210 and 1550  $\text{cm}^{-1}$ ). The three IR spectra are identical.

Interestingly, the three IR spectra of the protonated trisaccharides of the  $\text{Le}^y$ -series do not show any absorption bands around 1500  $\text{cm}^{-1}$ . Weak absorptions are, especially in larger molecules, difficult to resolve in the experiment. To examine which absorptions are theoretically found in the presented higher wavenumber regime, a model compound featuring a secondary amide group was used. The simplest molecule with a *trans*-amide group is *N*-methylacetamide. *N*-methylacetamide is well understood in the normal mode analysis of polypeptide backbone vibrations.<sup>[75-76]</sup> Strong N–H stretching vibrations  $\nu(\text{NH})$  are found at wavenumbers  $> 3000 \text{ cm}^{-1}$ . The amide I mode ( $\sim 1650 \text{ cm}^{-1}$ ) is defined as the C=O stretching

vibration  $\nu(\text{CO})$  with minor contributions of other modes. The amide II band ( $\sim 1550 \text{ cm}^{-1}$ ) is mainly the N–H in plane bending  $\delta(\text{NH})$  with contributions of the C–N stretching motion  $\nu(\text{CN})$  and other minor contributions. The amide I and amide II vibrations are depicted in Figure 15. The more complex amide III band is found between  $1200$  and  $1400 \text{ cm}^{-1}$ . Weak skeletal stretches are found at even lower wavenumbers ( $880\text{--}1200 \text{ cm}^{-1}$ ).

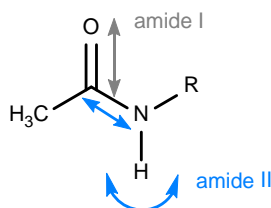


Figure 15: Important molecular vibrations in secondary amides such as in any HexNAc-containing saccharides between  $\sim 1500$  and  $\sim 1700 \text{ cm}^{-1}$ : the amide I (grey) mainly C=O stretching vibration  $\nu(\text{CO})$  and the amide II (blue) mainly the N–H in plane bending  $\delta(\text{NH})$  with contributions of the C–N stretching motion  $\nu(\text{CN})$ .

The given wavenumbers consider a neutral *N*-methylacetamide molecule. The amide group in the investigated glycans, however, has the highest gas-phase proton affinity or basicity. The location of the proton within the amide group is the oxygen atom.<sup>[77]</sup> The absorptions for the model compound *N*-methylacetamide shift with protonation. Calculations of protonated *N*-methylacetamide (see appendix) show that the amide I band shifts to lower wavenumbers ( $< 1600 \text{ cm}^{-1}$ ) with protonation at the oxygen and the amide II band shifts to higher wavenumbers ( $> 1700 \text{ cm}^{-1}$ ). For the protonated species of the *Le*<sup>y</sup>-series (Figure 14), bands  $< 1600 \text{ cm}^{-1}$  are most likely related to the amide I band, the C=O stretching vibration  $\nu(\text{CO})$  and the band around  $1662 \text{ cm}^{-1}$  to the amide II vibration. A band  $< 1600 \text{ cm}^{-1}$  can either not be detected because it is too weak with protonation of the oxygen or the broad band at  $1662 \text{ cm}^{-1}$  consists of both bands, the shifted amide I and the amide II vibration.

In the spectra in Figure 16, the trisaccharide standards from the Le<sup>b</sup>-series, Le<sup>a</sup> and BG-H1 measured as protonated species are compared to the fragmented Le<sup>b</sup> protonated ion. In general, the three spectra are rather congested and do not display many well-resolved peaks. In the spectrum of Le<sup>a</sup>, an assembly of broad peaks is found between 1050 and 1100 cm<sup>-1</sup>. In the same region, the spectrum of BG-H1 shows a broad peak with a maximum at about 1088 cm<sup>-1</sup> that has a different and smoother peak form. Further, there are three weaker absorptions between 1045 and 1200 cm<sup>-1</sup>. In the last part of both spectra, a more complex assembly of bands is present. This assembly of bands in the amide region likely indicates the occurrence of several chemical structures and/or conformations.

The IR spectra of Le<sup>a</sup> and BG-H1 as protonated ions are similar but distinguishable. They are further similar to the spectrum of the fragmented Le<sup>b</sup> protonated ion. With regards to the previous set of protonated glycan ions, this shows that either a fucose migration reaction is inhibited or the products of a possible migration reaction for Le<sup>a</sup> and BG-H1 are different. A fucose migration to more than one product structure is also possible. Tandem MS spectra were recorded for the two protonated trisaccharides (see appendix). Products of fucose migration with IRL are observable for BG-H1.

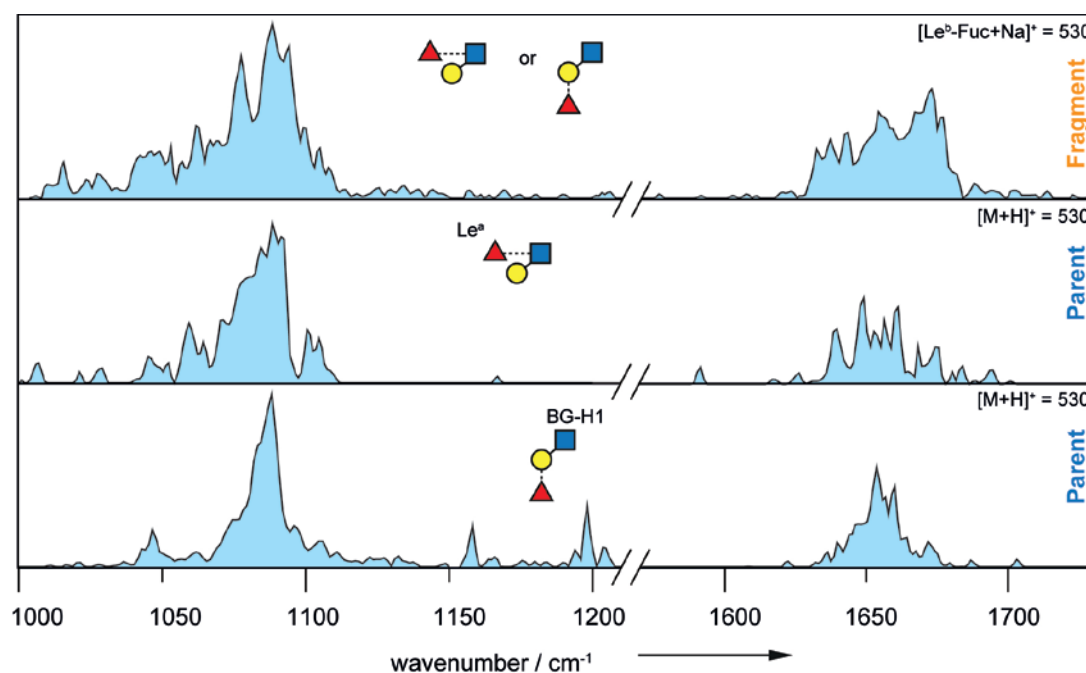


Figure 16: IR spectra of the fragment ion Le<sup>b</sup>-Fuc (upper panel) and the parent ions Le<sup>a</sup> (middle panel) and BG-H1 (lower panel) investigated as [M+H]<sup>+</sup> species in the range of 1000–1730 cm<sup>-1</sup> (break between 1210 and 1550 cm<sup>-1</sup>). The three IR spectra are identical.

To investigate the impact of reducing end modifications on fucose migration reactions, the reduced glycans Le<sup>x</sup>-ol and BG-H2-ol were synthesized. The cold-ion IR spectra of the intact ions as [M+H]<sup>+</sup> species are shown in Figure 17. Compared to the spectra of Le<sup>x</sup> and BG-H2, the spectra are not rich in distinct bands and share only four distinct features. The absorptions in the spectrum of Le<sup>x</sup>-ol are a subset to the absorptions in the spectrum of BG-H2-ol.

The spectrum of Le<sup>x</sup>-ol shows one strong well-resolved peak at 1095 cm<sup>-1</sup> and mainly two weaker absorptions between 1100 and 1200 cm<sup>-1</sup>. In the last part of the spectrum, a broad band appears between 1715 and 1750 cm<sup>-1</sup>. Compared to the absorption in amide I region of Le<sup>x</sup>, the band is shifted by about 75 cm<sup>-1</sup>. The

spectrum of BG-H2-ol shows, besides the absorptions of Le<sup>x</sup>-ol, a weaker absorption at 1048 cm<sup>-1</sup> and a strong absorption at 1084 cm<sup>-1</sup> next to the band at 1090 cm<sup>-1</sup> to form a split band. In the higher wavenumber regime, another broad peak appears between 1675 and 1710 cm<sup>-1</sup>. The highly widespread absorptions in the last part of both spectra can again indicate that several chemical structures and/or conformations are found in the spectrum of the molecules.

To summarize, the alditols can be easily distinguished from their non-reduced forms ( $\Delta m/z$  2) by their IR fingerprints. The spectra of both alditols most likely consist of more than one chemical structure and/or conformation. All absorptions of Le<sup>x</sup>-ol in the region of 1000 to 1800 cm<sup>-1</sup> are found in the spectrum of BG-H2-ol. This indicates that a subset of the gas-phase chemical structures of BG-H2-ol is identical to the gas-phase structure of Le<sup>x</sup>-ol. A possible explanation is an incomplete interconversion of BG-H2-ol to the gas-phase structure of Le<sup>x</sup>-ol. Also possible is that Le<sup>x</sup>-ol rearranges to a third gas-phase structure whereas BG-H2 rearranges to either more than one, of which one is identical to Le<sup>x</sup>-ol or incompletely to a third structure that is again identical to Le<sup>x</sup>-ol. It can be concluded that the reducing end modification in Le<sup>x</sup> and BG-H2 has an impact on the migration reaction and the sets of accessed gas-phase structures in the two spectra are partially different.

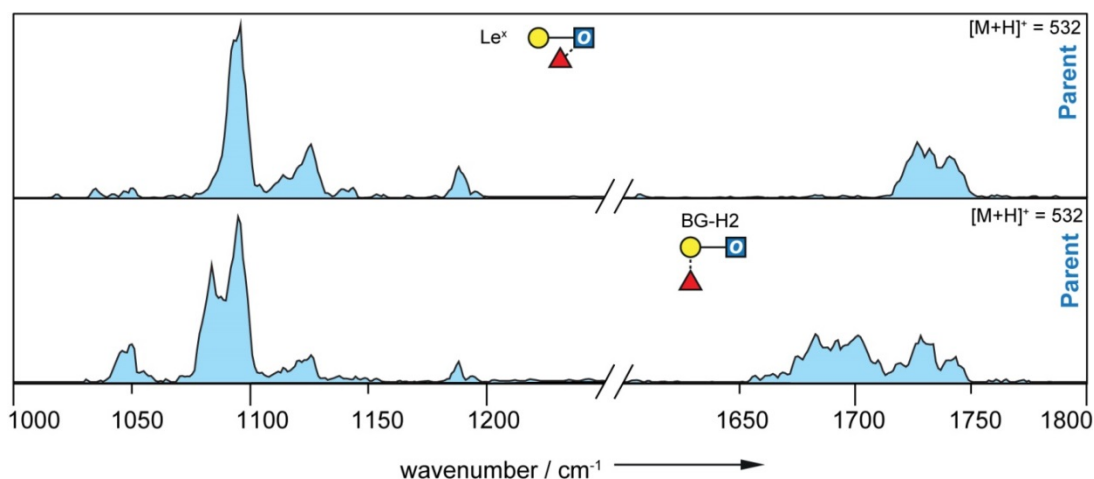


Figure 17: IR spectra of the parent ions  $\text{Le}^x$ -ol (upper panel) and BG-H2-ol (lower panel) investigated as  $[\text{M}+\text{H}]^+$  species in the range of 1000–1800  $\text{cm}^{-1}$  (break between 1250 and 1600  $\text{cm}^{-1}$ ). The two IR spectra are different but the IR spectrum of BG-H2-ol shows all features of the spectrum of  $\text{Le}^x$ -ol.

#### 4.1.3 AMMONIUM ADDUCT IONS

The next investigated adduct ions are the ammonium adduct ions of the trisaccharides from both blood group series. It has been reported that ammonium ions promote fucose migration reactions.

The IR spectra of the  $\text{Le}^y$ -series in Figure 18 display a large number of well-resolved features. The first part of the spectrum of BG-H2 shows at least nine well-resolved bands, partially of very sharp shape. The highest absorptions in the spectrum of BG-H2 are at 1045, 1075 and 1089  $\text{cm}^{-1}$ . Around 1500  $\text{cm}^{-1}$ , absorption bands are not detectable. A broad absorption decorates the higher wavenumber regime of the spectrum around 1660  $\text{cm}^{-1}$ . In the case of  $\text{Le}^x$ , the IR spectrum is not as well-resolved what might be due to slightly differing measurement conditions. Nevertheless, the spectrum is reproducible and averaged, as described in chapter 3.1. The spectrum shows all bands that are present in the spectrum of BG-H2 as

$[M+NH_4]^+$  adduct ion with varying intensities. All in all, the two spectra are almost identical considering the peak positions.

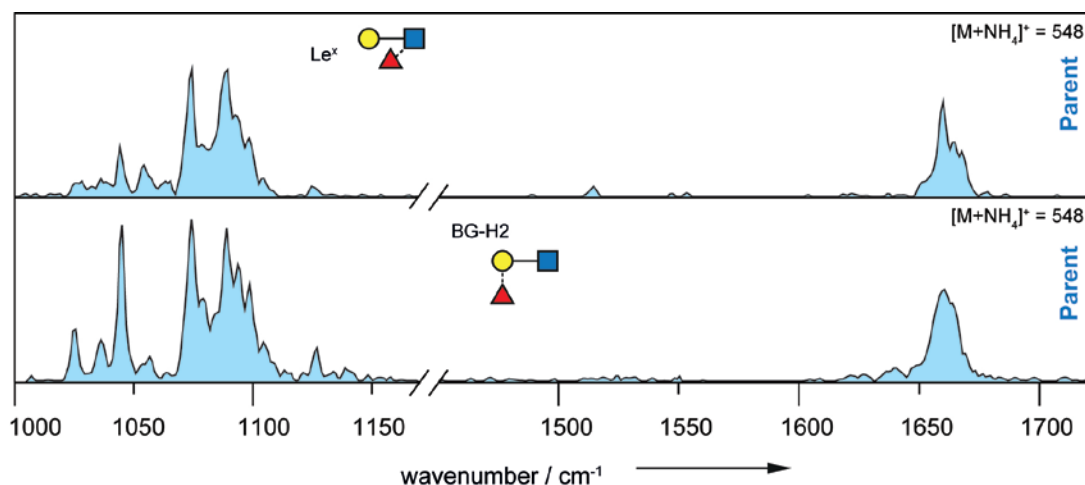


Figure 18: IR spectra of the parent ions  $Le^x$  (upper panel) and BG-H2 (lower panel) investigated as  $[M+NH_4]^+$  species in the range of 1000–1720  $cm^{-1}$  (break between 1170 and 1450  $cm^{-1}$ ). The two IR spectra are identical.

Comparing the spectra of different adducts within the  $Le^y$ -series, an interesting observation is made: the spectra of the  $[M+NH_4]^+$  and of the  $[M+H]^+$  species of  $Le^x$  and BG-H2 are identical. The stacked overlay in Figure 19 proves that the main features are present in all spectra (indicated by vertical dashed lines).

Typically, a different adduct ion attached to a glycan is expected to change the gas-phase conformation of the molecule to some extent and hence the IR spectrum, as seen in the spectra of the sodium adduct ions and the protonated ions. A possible explanation for the similarities in these spectra is that the observed species are not an ammonium adduct of a glycan  $[M+NH_4]^+$  but a neutral ammonia adduct of a protonated glycan  $[NH_3+MH]^+$ . In the latter, a proton shifts to the glycan and the ammonia is coordinated as a neutral species. With only weak interactions of the  $NH_3$ , the observed absorptions can be related to the protonated glycan.

The ion signal on the second TOF was evaluated for ammonia ( $\text{NH}_3$ ) loss, recorded as  $[\text{M}+\text{H}]^+$  ions and is shown in Figure 20.  $\text{NH}_3$  loss can be an indicator for the  $[\text{NH}_3+\text{MH}]^+$  adduct ion species. The  $\text{NH}_3$  loss is relatively high over all single scans, between 30% and > 100% of the height of the  $[\text{M}+\text{NH}_4]^+$  ion signal. Still, the  $\text{NH}_3$  loss depends on several parameters and is not directly comparable between different scans. The most important parameters are the laser energy, the focus (photon density) and the absorption strength (e.g. absorptions in the lower wavenumber region *vs.* the higher wavenumber region).

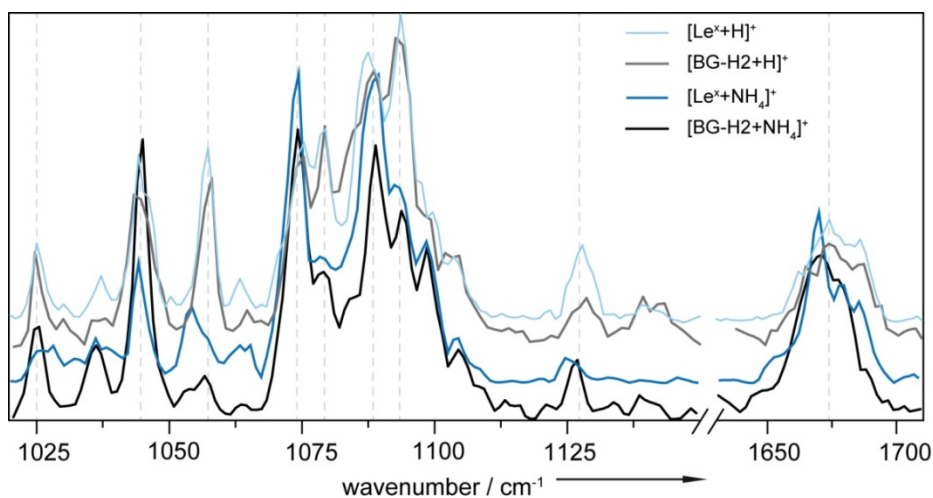


Figure 19: Stacked overlay of the IR spectra of the parent ions  $\text{Le}^x$  and BG-H2 investigated as  $[\text{M}+\text{H}]^+$  and  $[\text{M}+\text{NH}_4]^+$  species in the range of 1020–1710  $\text{cm}^{-1}$  (break between 1150 and 1640  $\text{cm}^{-1}$ ). The four IR spectra are identical.



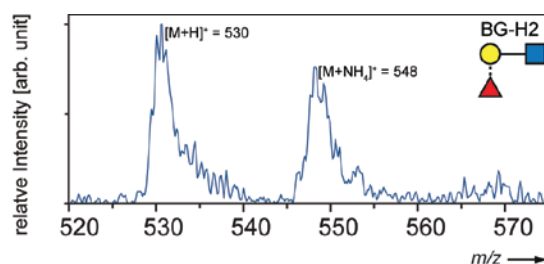


Figure 20: Ion signal [arb. unit] measured on the second TOF in a single scan of  $[BG-H2+NH_4]^+$  between 1000–1200  $cm^{-1}$ . Ammonia loss is found. It is important to emphasize that the ion signal of the protonated adduct ion is not part of the resulting IR spectrum.

Coming to the IR spectra of the trisaccharides of the  $Le^b$ -series as  $[M+NH_4]^+$  adducts, it immediately becomes apparent that these are not identical. In the spectrum of  $Le^a$  in Figure 21, roughly five low intensity bands are found between 1000 and 1050  $cm^{-1}$ . From 1050 to 1100  $cm^{-1}$ , two stronger features with red-shifted medium intensity features form a more congested peak pattern that is followed by another medium intensity peak at 1110  $cm^{-1}$ . The spectrum of  $Le^a$  shows a medium intensity peak at about 1520  $cm^{-1}$ . In the last part of the spectrum, three broad absorption bands in the range from 1625 to 1680  $cm^{-1}$  are present. The spectrum of BG-H1 shows four strong absorptions from 1040 to 1100  $cm^{-1}$  followed by a weak and not well-defined peak around 1110  $cm^{-1}$ . In the middle part of the spectrum, no absorptions are found. The last part of the spectrum shows, similar to  $Le^a$ , mainly three broad absorption bands but with different relative intensities in the range from 1625 to 1680  $cm^{-1}$ . Both spectra have well-resolved, but dissimilar features. Furthermore, they are different from the spectra of the protonated adducts of the  $Le^b$ -series.

The amount of  $NH_3$  loss was evaluated for  $Le^a$  and BG-H1. Over all scans, the  $NH_3$  loss, detected as  $[M+H]^+$  ions, is roughly between 0 and 75% of the height of the

$[M+NH_4]^+$  peak. Despite the mentioned restrictions concerning the comparability, it can be said that the  $NH_3$  loss is lower for the ammonium adducts of the  $Le^b$ -series than for the ammonium adducts of the  $Le^y$ -series.

To summarize, the difference of the spectra of the protonated ions and the ammonium adduct ions suggests that the gas-phase structures of the trisaccharides of the  $Le^b$ -series are different among each other and different with changing adduct ion. The lower extent of  $NH_3$  loss indicates that the observed structures in the spectra in Figure 21 are of  $[M+NH_4]^+$ -type.

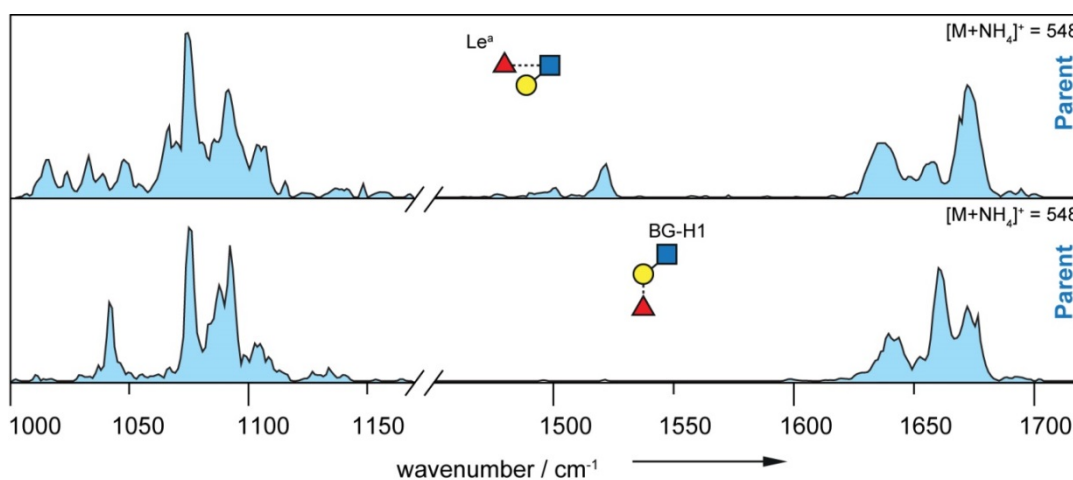


Figure 21: IR spectra of the parent ions  $Le^b$  (upper panel) and BG-H1 (lower panel) investigated as  $[M+NH_4]^+$  species in the range of 1000–1720  $cm^{-1}$  (break between 1170 and 1450  $cm^{-1}$ ).

#### 4.1.4 ALKYL AMMONIUM ADDUCT IONS

To further verify that the observed spectra of the ammonium adducts of the  $Le^y$ -series result from a  $[NH_3+MH]^+$ -type adduct ion, the IR spectra of two alkyl ammonium adduct ions were measured. Comparing the deprotonated equivalents, trimethylammonia (227 kcal/mol) and triethylammonia (235 kcal/mol) have higher

gas-phase proton affinities than ammonia (204 kcal/mol).<sup>[78-79]</sup> Therewith, a proton shift from the nitrogen to the glycan becomes more unlikely to occur.

The spectra of  $[\text{Le}^x + \text{NMe}_3\text{H}]^+$  and  $[\text{Le}^x + \text{NEt}_3\text{H}]^+$  in Figure 22 are almost identical, but different from the spectrum of  $[\text{Le}^x + \text{NH}_4]^+$ . Differences in the two spectra are a side peak at  $1081\text{ cm}^{-1}$  in the spectrum of  $[\text{Le}^x + \text{NMe}_3\text{H}]^+$  and the feature in the higher wavenumber range is shifted for  $[\text{Le}^x + \text{NMe}_3\text{H}]^+$  by  $3\text{ cm}^{-1}$ . Both spectra of the alkyl ammonium adducts show two well-resolved bands at  $1050\text{ cm}^{-1}$  and at  $1085\text{ cm}^{-1}$  of which the first is a split peak. At  $1515\text{ cm}^{-1}$  and  $1540\text{ cm}^{-1}$ , the spectra of  $[\text{Le}^x + \text{NMe}_3\text{H}]^+$  and  $[\text{Le}^x + \text{NEt}_3\text{H}]^+$  show two weak bands. In the higher wavenumber range, a peak is found which is slightly blue-shifted to the feature in the spectrum of the ammonium adduct species.

The theoretical spectrum of a trimethylammonium ion was calculated, to possibly show that the observed absorptions originate from the glycan and not from the adduct ion. The calculated absorptions are provided within the appendix. The main absorptions for trimethylammonium are around  $1000\text{ cm}^{-1}$ ,  $1500\text{ cm}^{-1}$  and  $3500\text{ cm}^{-1}$ . The vibrations of a trimethylammonium ion most likely shift with coordination of another molecule. Still, the main absorptions do not overlap with the absorptions in the experimental spectrum of  $[\text{Le}^x + \text{NMe}_3\text{H}]^+$ .

In summary, the spectra of trimethylammonium and triethylammonium adducts of  $\text{Le}^x$  are similar. The gas-phase structure of  $\text{Le}^x$  are, therefore, very similar with the increasing length of the alkyl chains in the adduct ion. However, the difference to the spectrum of the ammonium adduct is apparent. The gas-phase chemical structures and/or conformations of the alkyl ammonium adducts of  $\text{Le}^x$  are similar whilst the chemical structures and/or conformations of the ammonium adduct of  $\text{Le}^x$  is identical to the protonated species.

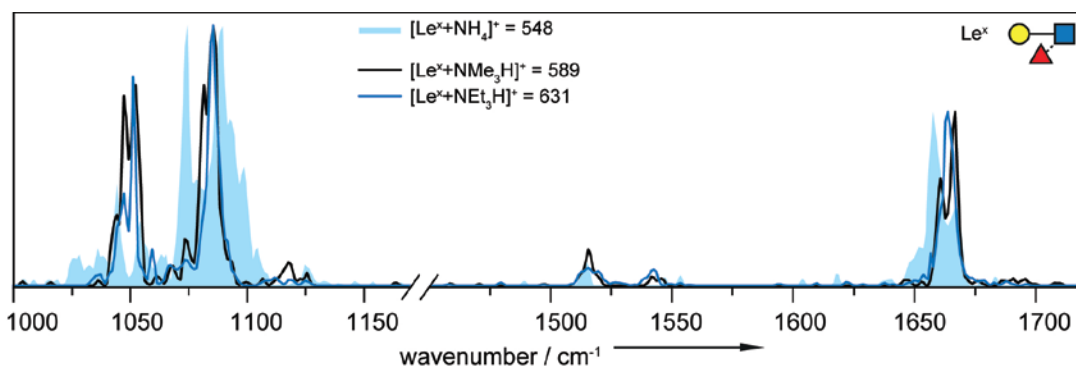


Figure 22: Overlay of the IR spectra of  $[\text{Le}^x+\text{NMe}_3\text{H}]^+$  (black line) and  $[\text{Le}^x+\text{NEt}_3\text{H}]^+$  (blue line) as parent ions with the IR spectrum of  $[\text{Le}^x+\text{NH}_4]^+$  (blue filled) also as parent ion in the range of 1000–1720  $\text{cm}^{-1}$  (break between 1170 and 1450  $\text{cm}^{-1}$ ). The spectra of the alkyl ammonium adducts are very similar and different from the spectrum of the ammonium adduct of  $\text{Le}^x$ .

#### 4.1.5 HYDROGEN-DEUTERIUM EXCHANGE EXPERIMENT

In trisaccharides, the assignment of vibrational modes is challenging because of the large size of the molecule and therefore complexity of vibrational modes. A hydrogen-deuterium exchange experiment was performed for the protonated species of  $\text{Le}^x$  to potentially assign the vibrational mode around 1662  $\text{cm}^{-1}$ . Vibrational modes that are typical for the wavenumber regime are the amide I and amide II mode and also the O–H stretching vibration,  $\nu(\text{OH})$  from the proton at the oxygen of the amide group.

On average, eight hydrogens exchanged in the observed ions and the trapping times were kept at a few seconds to lower the extent of back exchange in the ion trap. The band around 1662  $\text{cm}^{-1}$  in the spectrum of  $[\text{Le}^x+\text{H}]^+$  exhibits a red-shift in the spectrum of  $[\text{Le}^x\text{-D+D}]^+$  by almost 20  $\text{cm}^{-1}$ . This observation strengthens the assumption that this band is related to the vibrations of the amide group.

Theoretical calculations were performed for the model compound *N*-methylacetamide as protonated species and deuterated species (see appendix). The protonation site is the oxygen atom.<sup>[77]</sup> In the deuterated molecule, two hydrogen atoms are exchanged. The amide I band shifts by  $64\text{ cm}^{-1}$  to lower wavenumbers and the amide II band shifts by  $13\text{ cm}^{-1}$  to lower wavenumbers. The vibration of the proton or deuteron at the oxygen shifts with exchange by more than  $1000\text{ cm}^{-1}$ . The comparability of the model compound to the vibrations in the trisaccharide is limited because of the impact of a hydrogen bonding network in the trisaccharide. Nevertheless, it can be ruled out that the experimentally observed vibrational mode around  $1662\text{ cm}^{-1}$  is the O–H stretching  $\nu(\text{OH})$  of the proton at the protonation site but without further theoretical calculations, it cannot be differentiated between the amide I and amide II band.

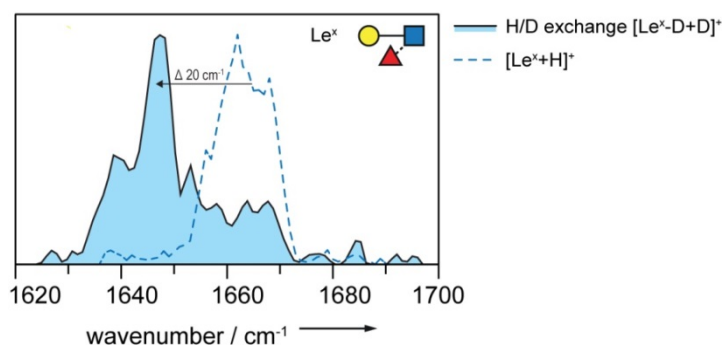


Figure 23: Overlay of the IR spectra of  $[\text{Le}^{\text{x}}+\text{H}]^+$  (dashed blue line) and  $[\text{Le}^{\text{x}}-\text{D}+\text{D}]^+$  (blue filled) observed in a hydrogen-deuterium exchange experiment in the range of  $1620\text{--}1700\text{ cm}^{-1}$ . The band shifts by almost  $20\text{ cm}^{-1}$ .

#### 4.1.6 PRECOOLED GLYCAN IONS

To investigate the location of ion activation in the instrument and the effect of long trapping times, the trisaccharides  $\text{Le}^{\text{x}}$  and BG-H2 as protonated species were thermalized to about  $80\text{ K}$  inside the trap before they were embedded in superfluid

helium droplets (0.4 K). In general, ions embedded in superfluid helium droplets are expected to be kinetically trapped. At temperatures near 0 K, nearly all molecular motion discontinues. The cooling rate is most likely so high that in this time the molecules cannot convert to their lowest energy structure. Therefore, the distribution of different chemical structures and their conformations equals the distribution before pick-up. By cooling the ion trap, the distribution of possible structures present in the IR spectrum can change. With this, molecular kinetic properties can be determined and slower gas-phase reactions are possibly inhibited.

The IR spectra of  $\text{Le}^x$  and BG-H2 with use of the cooled trap are given in Figure 24. The underlying, red filled traces show the measurement of the same ions without precooling for comparison. The spectrum of  $\text{Le}^x$  does not change with precooling. All bands are highly reproducible. On the contrary, the spectrum of BG-H2 with use of the cooled trap slightly changes. Most importantly, the feature in the last part of the spectrum is broadened. It is more than twice the FWHM of the band without use of the cooled trap. This indicates that with precooling of the ions more chemical structures and/or conformations are accessed in the spectrum. In addition, two bands in the lower wavenumber regime show a much lower intensity. This can also be attributed to a change in the ratio of conformations present.

It can be concluded that cooling partially inhibits a gas-phase reaction for BG-H2. In the spectrum of BG-H2 with precooling of the ions, the set of conformers changes and/or more chemical structures are present. The latter can be a mixture of educts and products or intermediate chemical structures in the migration of a fucose unit. For  $\text{Le}^x$ , a migration reaction cannot be ruled out. The reaction rate could be too high to detect multiple chemical structures in the IR spectrum. As discussed in chapter 4.1.2, the trisaccharides  $\text{Le}^x$  and BG-H2 have the same chemical structures after the

migration reaction. The chemical structure is either a third structure or one of the trisaccharides interconverts to the other. With this experiment, it becomes more likely that BG-H2 interconverts to  $\text{Le}^x$ . The first possibility can, nonetheless, not be excluded.

To answer the question of the place of activation within the instrument, the experiment shows that the ions are not activated in the trap but at earlier stages of the instrument. With cooling of the ion trap, the migration reaction for BG-H2 can partially not proceed to the final chemical structure. The front end of the instrument consists of a commercial source region (Q-TOF Ultima, *Waters Corporation*) with a nESI source which is known to be a particularly soft ionization interface. Therefore, the ions are most likely activated while transferred into the instrument.

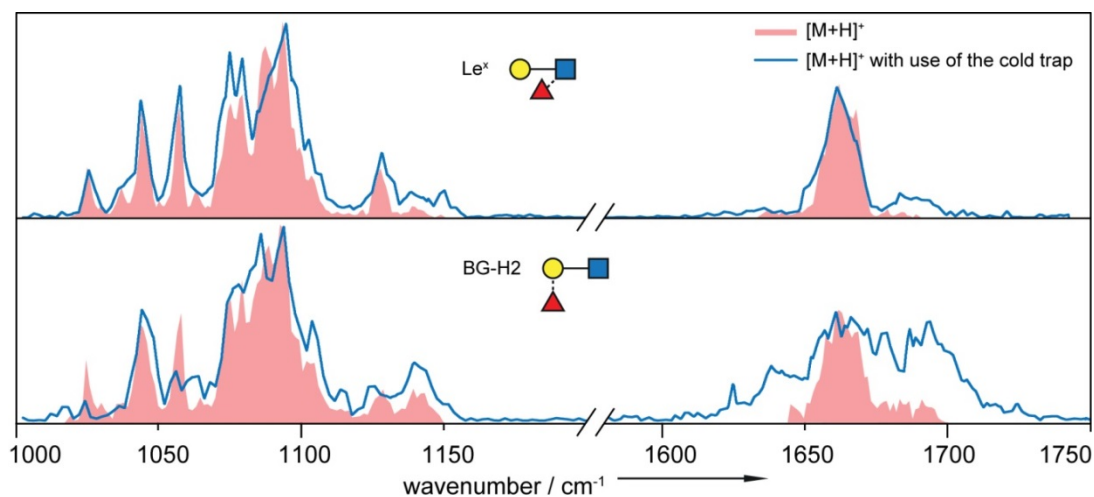


Figure 24: Overlay of the IR spectra of  $\text{Le}^x$  (upper panel) and BG-H2 (lower panel) as  $[\text{M}+\text{H}]^+$  ions with use of the cooled trap (blue spectral line) and without use of the cooled trap (red filled) in the range of 1000–1750  $\text{cm}^{-1}$  (break between 1200 and 1580  $\text{cm}^{-1}$ ). The spectrum of BG-H2 changes with the change in experimental conditions, whereas the spectrum of  $\text{Le}^x$  is identical in both measurements.

## 4.2 ION MOBILITY-MASS SPECTROMETRY

Ion mobility-mass spectrometry (IM-MS) experiments were performed to obtain the collision cross sections (CCS) of the investigated glycans and to investigate the role of soft in-source activation. A brief introduction to IM-MS and a detailed description of the experimental setups is found in chapter 3.2.

In literature, sodium adducts of Lewis and blood group carbohydrates epitopes are reported to be partially distinguishable with IM-MS.<sup>[30]</sup> For the isomeric trisaccharides  $m/z$  552 of the Le<sup>y</sup>-series (Le<sup>x</sup> and BG-H2), distinct CCSs are obtained, whereas the trisaccharides  $m/z$  552 of the Le<sup>b</sup>-series (Le<sup>a</sup> and BG-H1) are not separable. Nevertheless, the latter do not have the same chemical structure as shown with their distinct IR fingerprint spectra (chapter 4.1.1).

### 4.2.1 IM-MS RESULTS

The experimental CCSs are given in Table 3 with the corresponding ion type, charge and mass-to-charge ratio. All ions were measured as protonated species and the Lewis and blood group epitopes were also investigated as  $[M+NH_4]^+$  and  $[M+NEt_3H]^+$  adduct ions. In case of multiple peaks in the arrival time distribution of one ion, the additional peaks are given within the same line and in case of side peaks, they are given in brackets.



Table 3: Absolute collision cross section values [in Å<sup>2</sup>] for the investigated glycans (chapter 2.3) given with corresponding ion type, charge, charge carrier and mass-to-charge ratio ( $m/z$ ). Drift tube (DT) ion mobility-mass spectrometry measurements with helium (He) drift gas were performed on a Synapt G2Si instrument (*Waters Corporation*) (grey shaded) or on a home-built drift tube device (blank background), alternatively. The standard deviation derived from the linear regression analysis is max. 1%.

Substance	Ion Type	Charge	Charge Carrier	$m/z$	<sup>DT</sup> CCS <sub>He</sub> [Å <sup>2</sup> ]*
Le <sup>y</sup> -Fuc	Fragment	1	[M+H] <sup>+</sup>	530	142
Le <sup>b</sup> -Fuc	Fragment	1	[M+H] <sup>+</sup>	530	141
Le <sup>x</sup>	Parent	1	[M+H] <sup>+</sup>	530	141
Le <sup>a</sup>	Parent	1	[M+H] <sup>+</sup>	530	141
BG-H2	Parent	1	[M+H] <sup>+</sup>	530	142
BG-H1	Parent	1	[M+H] <sup>+</sup>	530	141
Le <sup>x</sup>	Parent	1	[M+NH <sub>4</sub> ] <sup>+</sup>	548	142
Le <sup>a</sup>	Parent	1	[M+NH <sub>4</sub> ] <sup>+</sup>	548	144 (148)
BG-H2	Parent	1	[M+NH <sub>4</sub> ] <sup>+</sup>	548	149
BG-H1	Parent	1	[M+NH <sub>4</sub> ] <sup>+</sup>	548	146
Le <sup>x</sup>	Parent	1	[M+NEt <sub>3</sub> H] <sup>+</sup>	631	165
BG-H2	Parent	1	[M+NEt <sub>3</sub> H] <sup>+</sup>	631	165, 171
Le <sup>x</sup> -ol	Parent	1	[M+H] <sup>+</sup>	532	144
BG-H2-ol	Parent	1	[M+H] <sup>+</sup>	532	144
2'-FL	Parent	1	[M+H] <sup>+</sup>	489	130
3'-FL	Parent	1	[M+H] <sup>+</sup>	489	136 (133)

A2XX-L	Parent	1	[M+H] <sup>+</sup>	632	162
A3XX-L	Parent	1	[M+H] <sup>+</sup>	632	166
XA2X-L	Parent	1	[M+H] <sup>+</sup>	632	171
XA3X-L	Parent	1	[M+H] <sup>+</sup>	632	155

\*The <sup>DT</sup>CCS<sub>He</sub> are given for the main peak or double peaks (with similar intensity). The <sup>DT</sup>CCS<sub>He</sub> of possible side peaks are given in brackets.

L: Linker

For the four protonated trisaccharides Le<sup>x</sup>, Le<sup>a</sup>, BG-H2 and BG-H1 and the fragment ions of Le<sup>y</sup> and Le<sup>b</sup> ( $m/z$  530), similar CCS are obtained (Le<sup>x</sup>: 141 Å<sup>2</sup>, Le<sup>a</sup>: 141 Å<sup>2</sup>, BG-H2: 142 Å<sup>2</sup>, BG-H1: 141 Å<sup>2</sup>, Le<sup>y</sup>-Fuc: 142 Å<sup>2</sup> and Le<sup>b</sup>-Fuc: 141 Å<sup>2</sup>). The deviation is within 1 Å<sup>2</sup>. Considering a standard deviation of < 1%, the CCS values are identical. In fragmentation analysis, the fragments of Le<sup>y</sup> and Le<sup>b</sup> as protonated ions could therefore not be identified. The arrival time distributions are given as an overlay in Figure 25.

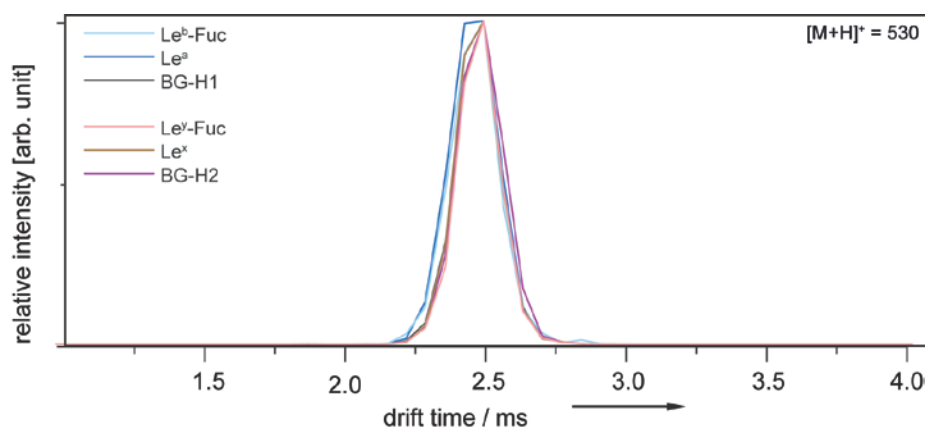


Figure 25: Overlay of arrival time distributions (ATDs) of the trisaccharides from Le<sup>y</sup>- and Le<sup>b</sup>-series measured as protonated species. Drift tube ion mobility-mass spectrometry measurements with helium drift gas were performed on a Synapt G2Si instrument (Waters Corporation). For each species, CCSs were determined.

To investigate the impact of reducing end modifications, the alditol forms of Le<sup>x</sup> and BG-H2 were analyzed with IM-MS. The reduced trisaccharides Le<sup>x</sup>-ol and BG-H2-ol are not separable with IM-MS. The CCSs for Le<sup>x</sup>-ol and BG-H2-ol as protonated ions ( $m/z$  532) are both 144 Å<sup>2</sup>.

The CCSs for Le<sup>x</sup> and BG-H2 as ammonium adducts ( $m/z$  548) are 142 Å<sup>2</sup> and 149 Å<sup>2</sup>, respectively. The difference of 7 Å<sup>2</sup> is significant, considering that they yield identical IR spectra (chapter 4.1.3). For the triethylammonium adduct species of Le<sup>x</sup> and BG-H2 ( $m/z$  631) CCSs of 165 Å<sup>2</sup> and 165 Å<sup>2</sup>, 171 Å<sup>2</sup> are obtained, respectively. The arrival time distribution for BG-H2 ( $m/z$  631) shows two distinct peaks ( $\Delta t$  0.4 ms) which are not baseline-separated.

Le<sup>a</sup> as ammonium adduct ( $m/z$  548) exhibits a CCS of 144 Å<sup>2</sup> for the main peak. A side peak is found at longer drift time with a CCS of 148 Å<sup>2</sup>. The ammonium adduct of BG-H1 ( $m/z$  548) results a CCS of 146 Å<sup>2</sup>.

To interrogate the function of the secondary amide group on fucose migration reactions in Le<sup>x</sup> and BG-H2, two fucosylated milk sugars were investigated with IM-MS. 3'-FL and 2'-FL are structurally similar to Le<sup>x</sup> and BG-H2 with Glc instead of GlcNAc. With the lack of the amide group, the excess proton is less localized. For the protonated milk sugars ( $m/z$  489), distinct CCSs are obtained. The two peaks are discernible but not baseline-separated. For 3'-FL, a side peak at shorter drift time is found. The deviation of the drift times of the main species of 3'-FL and 2'-FL is almost 0.3 ms and the deviation of the CCS is 6 Å<sup>2</sup>. In Figure 26, the arrival time distributions are shown. The lack of the secondary amide group likely inhibits a migration reaction for the two milk sugars.

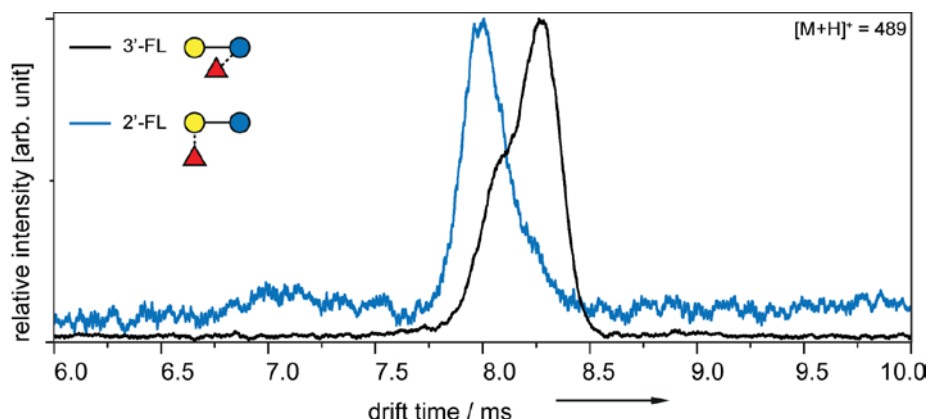


Figure 26: Overlay of arrival time distributions (ATDs) of 3'-FL (black) and 2'-FL (blue) measured as protonated species. Drift tube ion mobility-mass spectrometry measurements with helium drift gas were performed on a home-built device. For each species, CCSs were determined. The ionization of 2'-FL is not as good as the ionization of 3'-FL.

In the most recent publication on IRL (chapter 2.4), the migrating residue is a xylopyranose monosaccharide. The non-fucosylated glycans in this work, therefore, also carry differently linked, terminal aldopentose residues, here arabinoses, that have a furanose ring-form. The four isomeric plant sugars A2XX, A3XX, XA2X and XA3X as protonated ions ( $m/z$  632) are separable with IM-MS. The CCS values of XA2X ( $171 \text{ \AA}^2$ ) and XA3X ( $155 \text{ \AA}^2$ ) differ by  $16 \text{ \AA}^2$ . The two peaks are nearly baseline-separated. For A2XX and A3XX, the obtained CCSs are  $162 \text{ \AA}^2$  and  $166 \text{ \AA}^2$ , respectively. The arrival time distributions are shown in Figure 27. The four isomeric glycans with arabinofuranose residues do not indicate the occurrence of migration reactions to the same structure. Nevertheless, with this experimental approach, a migration reaction cannot be fully ruled out because the resulting chemical structures can also be different.

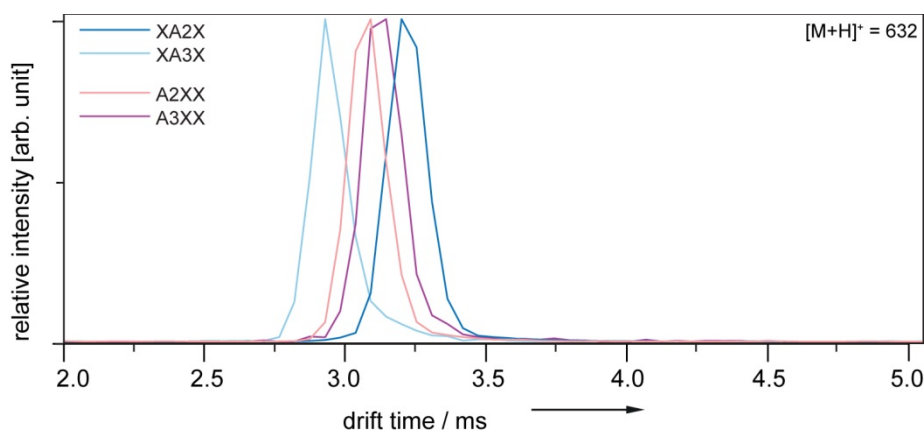


Figure 27: Overlay of arrival time distributions (ATDs) of the arabinoxyranes (A2XX, A3XX, XA2X and XA3X) measured as protonated species. Drift tube ion mobility-mass spectrometry measurements with helium drift gas were performed on a Synapt G2Si instrument (*Waters Corporation*). For each species, CCSs were determined.

#### 4.2.2 PROBING SOFT IN-SOURCE ACTIVATION

Soft in-source activation experiments (on the home-built drift tube instrument) were performed to investigate the role of possible activation for a fucose migration reaction. The experiments were conducted for the Lewis and ABO blood group glycan ions as protonated and triethylammonium species as well as for the milk sugars as protonated ions.

An overlay of the arrival time distributions of  $\text{Le}^x$  (grey and black) and BG-H2 (light and dark blue) measured with lower and higher injection voltages (low: 122 V, high: 194 V) is given in Figure 28. With increasing injection voltage, the main peak for BG-H2 shifts to shorter drift time by about 0.2 ms. The arrival time distributions are of broad, multiple Gaussian peak shape. At lower injection voltage, a side peak is found at shorter drift time and at higher injection voltage, a side peak is found at longer drift time.  $\text{Le}^x$ , on the contrary, does not show any difference in drift time for

the main peak upon in-source activation. A broadening of the drift time peak was observable with higher injection voltage. Both drift time peaks for  $\text{Le}^x$  share a side peak at longer drift times. Comparing the arrival time distribution in Figure 25 measured on the Synapt G2Si instrument (*Waters Corporation*), the peak for BG-H2 is not shifted to longer drift time. Based on experience, this is due to the harsher source conditions of the commercial instrument.

The shape of the arrival time distribution of BG-H2 and also the resulting CCS of the main peak ( $143 \text{ \AA}^2$ ) at higher injection voltage are similar to the arrival time distribution and CCS ( $144 \text{ \AA}^2$ ) of  $\text{Le}^x$ . This indicates that BG-H2 interconverts to a gas-phase shape similar to  $\text{Le}^x$ . Still, a fucose migration reaction cannot be ruled out for  $\text{Le}^x$ . The energy barrier for  $\text{Le}^x$  could be even lower than the activation with the soft conditions on the home-built instrument. Nevertheless, this result further strengthens the assumption that BG-H2 interconverts to  $\text{Le}^x$  but a third structure as migration product can still not be excluded from the discussion. For the triethylammonium adducts of  $\text{Le}^x$  and BG-H2, the arrival time distributions do not differ with different injection voltages.

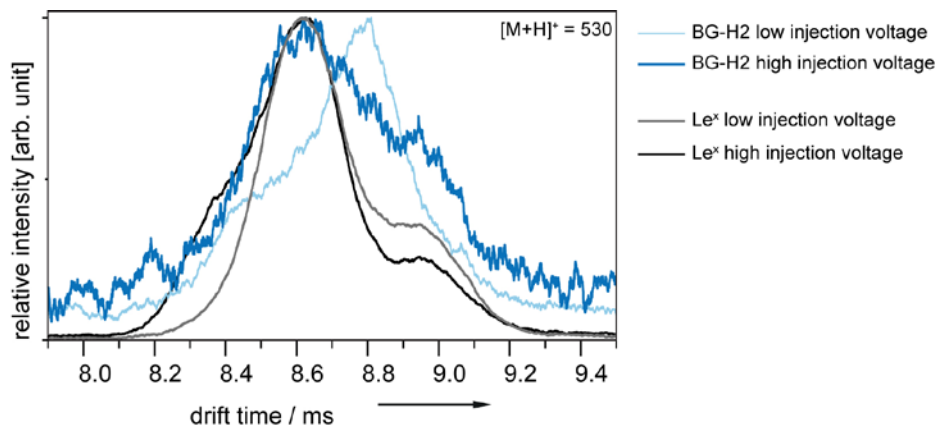


Figure 28: Overlay of arrival time distributions (ATDs) of  $\text{Le}^x$  (black) and BG-H2 (blue) measured as protonated ions with two injection voltages. Drift tube ion

mobility-mass spectrometry measurements with helium drift gas (He) were performed on a home-built device (chapter 3.2). The drift time of BG-H2 changes with the different injection voltages.

For Le<sup>a</sup> as protonated species, a very small shift of about 0.05 ms to longer drift time can be detected at higher injection voltage, but the peak form does not change. With the small variation in the drift time, an interpretation of the soft in-source activation experiment is not possible for Le<sup>a</sup>. The arrival time distribution of BG-H1 does not change with different injection voltages, but the peak broadens with higher injection voltage. This experiment does not give more insight into a possible fucose migration reaction for the trisaccharides of the Le<sup>b</sup>-series.

The protonated milk sugars 3'-FL and 2'-FL with peak-separated drift time peaks (Figure 26) do not show a difference with increasing injection voltage. At high injection voltages, the ions fragment and are not detectable anymore. The milk sugars do not indicate the occurrence of fucose migration with the given instrumental settings.

## 5 CONCLUSION AND OUTLOOK

The aim of this work was to investigate the gas-phase structures of fucosylated glycans with focus on the intramolecular migration of a fucose monosaccharide building block. With the combination of mass spectrometry and cold-ion IR spectroscopy, gas-phase IR spectra of fucosylated, biologically relevant glycan tri- and tetrasaccharide ions at 0.4 K were recorded.

The utility of the method for the analysis of fucose migration was proven with the IR spectra of a set of sodiated, isomeric ions of the Lewis and ABO blood group antigen systems. For sodiated glycan ions, fucose migration reactions have not been reported. Consistent with this result, the IR spectra of sodiated, fucose-containing trisaccharides presented in this work do not show evidence of fucose migration. Specifically, the IR spectra of singly fucosylated trisaccharides resulting from dissociation of doubly fucosylated tetrasaccharides  $\text{Le}^y$  and  $\text{Le}^b$  were measured. Two structures are possible for each trisaccharide product, corresponding to the two possible sites for loss of a fucose residue, with  $\text{Le}^x$  and BG-H2 the expected products of  $\text{Le}^y$  and  $\text{Le}^a$  and BG-H1 the expected products of  $\text{Le}^b$ . It was found that the IR spectra of the dissociation products of  $\text{Le}^y$  and  $\text{Le}^b$  correspond to a linear combination of the putative product spectra and suggest an approximate fragment ratio of 1:1 ( $\text{Le}^x$ :BG-H2 and  $\text{Le}^a$ :BG-H1).

In contrast to the spectra of sodiated glycan ions, the spectra obtained for glycan ions possessing a mobile proton are not consistent with prior studies. In previous literature, fucose migration reactions in singly or doubly protonated as well as ammonium adduct glycan ions have only been associated with CID. The terms fucose migration and IRL have been used interchangeably. In this thesis, identical IR spectra have been obtained for a set of isomeric, intact fucosylated trisaccharides.



This shows that fucose migration is not limited to fragment ions from IRL and occurs in intact glycan ions, independent of an internal loss. The results obtained in this thesis recommend a more precise wording for this phenomenon.

Observing fucose migration in intact glycan ions implies that the energy barrier for the migration reaction can be considerably lower than the barrier for dissociation. The magnitude of this barrier, however, cannot be generalized because it likely depends on the properties of the investigated glycan. The conditions in the experiments with intact glycan ions were optimized to minimize the extent of activation. Nevertheless, as in all mass spectrometers, activation of the ions occurs to some extent, especially during the transfer of the ions into the mass spectrometer. Further experiments are required to determine the effective temperature of the molecules at different instrument settings, for example using thermometer molecules.

The migration reaction reported here was observed in protonated ions as well as ammonium adducts of intact Le<sup>x</sup> and BG-H2. The gas-phase IR spectra of the intact ions Le<sup>x</sup> and BG-H2 as protonated ions are identical, suggesting identical gas-phase structures. Additional experiments examining the IR spectra of precooled ions and IM-MS drift times with variable in-source activation conditions potentially indicate that the isomeric trisaccharide BG-H2 with a (1→2)-linked fucose unit interconverts to Le<sup>x</sup>. It can, however, not be excluded that both trisaccharides migrate to a third common structure. In this scenario, the reaction rate of the fucose migration in Le<sup>x</sup> would be too high to observe any intermediate structures. Similar to the mechanism proposed by Harvey, *et al.*<sup>[49]</sup>, a possible mechanism for the migration of fucose in BG-H2 with an interconversion to Le<sup>x</sup> is suggested in Figure 29.

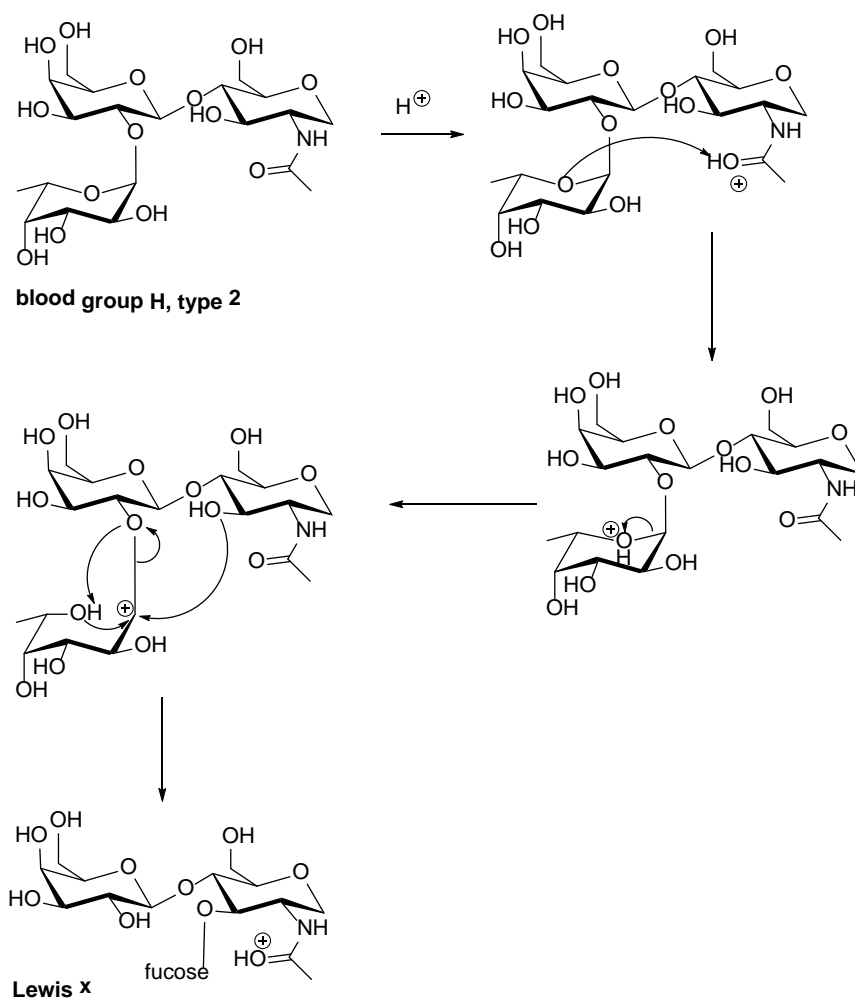


Figure 29: Possible mechanism for the migration of fucose in BG-H2 similar to the proposed mechanism in Harvey, *et al.*<sup>[49]</sup>. A possible explanation of the experimental results is that the product of the migration reaction is identical to the structure of the isomeric trisaccharide Le<sup>x</sup>.

Interestingly, the spectra of the protonated glycans Le<sup>x</sup> and BG-H2 were identical to the spectra of the respective ammonium adduct ions. In the ammonium adducts, the proton most likely shifted to the glycan to form a [MH+NH<sub>3</sub>]<sup>+</sup>-type adduct, which has an identical chemical structure and similar conformation to the protonated ion. The IR spectra of the alkyl ammonium adduct ions compared to the IR spectra of

ammonium adduct and protonated ion of  $\text{Le}^x$  indicate that the reaction requires a mobile proton located at the glycan.

The separation of the milk sugars 2'-FL and 3'-FL with IM-MS shows that the lack of a secondary amide functional group at the reducing-end monosaccharide inhibits a fucose migration reaction. The amide functional group in  $\text{Le}^x$  and BG-H2 can, thus, catalyze the fucose migration reaction. Possible explanations are that the proton is either directed by the secondary amide group to a proximal fucose glycosidic bond or that the proton is transferred through long hydrogen-bonded chains. Furthermore, the modification of the reducing end to an open chain alditol in  $\text{Le}^x$  and BG-H2 either partially inhibits or at least alters the migration reaction.

As an outlook, the IR spectrum of the protonated trisaccharide BG-H2 labelled with 2-aminobenzamide is shown in Figure 30. The two trisaccharides  $\text{Le}^x$  and BG-H2 can now serve an ideal system to study the influence of different linkers, adduct ions or variations in functional groups on fucose migration reactions.

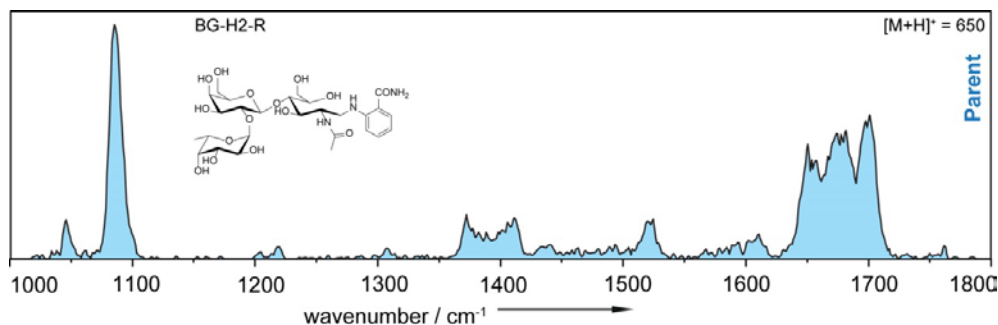


Figure 30: IR spectrum of BG-H2 with 2-aminobenzamide label (R) investigated as protonated parent ion in the range of 1000–1800  $\text{cm}^{-1}$ .

The IR spectra of the trisaccharides of the  $\text{Le}^b$ -series exhibited similar, but not identical spectral lines that were significantly broader than those observed for the  $\text{Le}^y$  series. It is possible that more than one set of chemical structures, each with

numerous conformational families, contributes to the spectrum. Fucose migration cannot be excluded in this series, as the broad bands observed greatly hinder analysis. A general drawback is that it is challenging to utilize the experimental data to identify any migration products that possess an unknown chemical structure.

In the literature, migration reactions have also been reported for other monosaccharides, e.g. the aldopentose monosaccharide xylose<sup>[56]</sup>. To potentially broaden the scope of the thesis, a set of isomeric non-fucosylated glycans that differed in the location of arabinose residues were investigated with IM-MS. For these samples, an indication of an aldopentose migration reaction could, yet, not be found. Future investigations need to examine which monosaccharides can undergo migration reactions. This is vital to assess whether the type of monosaccharide inhibits or enables a migration reaction or whether other structural properties, e.g. the linkage-type, are critical.

This thesis further illustrates the necessity for a multidimensional analysis of the intermediates and products of fucose migration reactions. Theoretical calculations are useful to match candidate chemical structures to an experimental spectrum and then possibly predict pathways for a migration reaction. For sodiated ions, strong agreement is observed between the preliminary theoretical results obtained by Mateusz Marianski (*Fritz Haber Institute, Berlin*, and now *City University of New York, New York*) and the experimental spectra. For protonated ions, more low-energy structures are usually found, and so far the match between theoretical and experimental vibrational spectra is not conclusive. Besides the large number of degrees of freedom mentioned in chapter 2.1 for glycans in the gas phase, the challenge in protonated glycans is to predict the connectivity of the fucose unit after migration, the protonation site and also the occurrence of multiple chemical

structures. Two low-energy structures and a linear combination of their vibrational spectra for protonated  $\text{Le}^\times$  have been calculated by Mateusz Marianski and are shown as preliminary results in Figure 31. The match between the experimental and theoretical spectrum is encouraging. Future experiments performing more extensive theoretical calculations, using hydrogen-deuterium exchange in IM-MS<sup>[80]</sup> or even site-specific isotope labeling are required to fully understand the underlying processes.

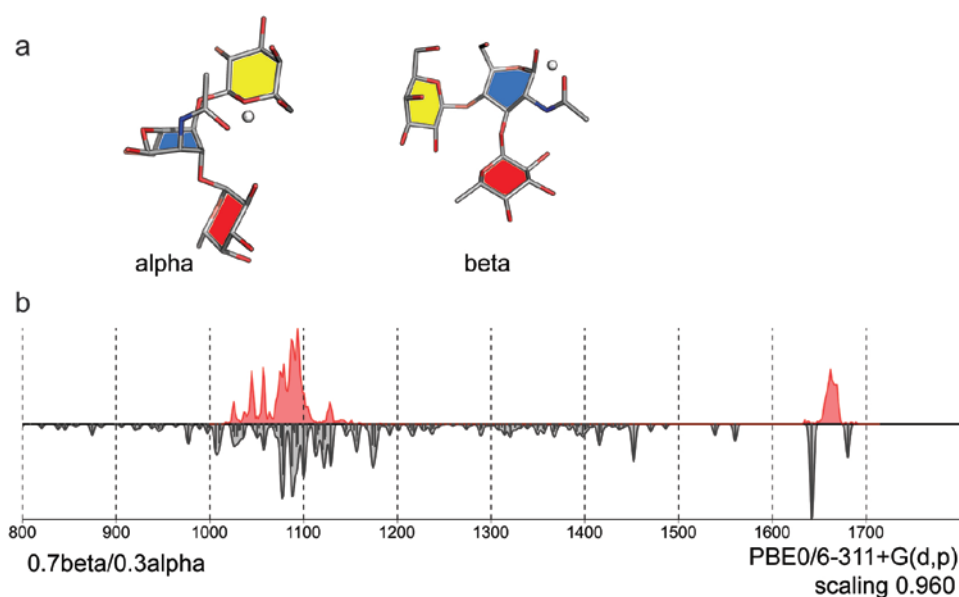


Figure 31: Preliminary theoretical results calculated by Mateusz Marianski (*Fritz Haber Institute, Berlin, and now City University of New York, New York*). a) Calculated low-energy structures for protonated  $\text{Le}^\times$  in alpha and beta configuration. b) Calculated IR spectrum for protonated  $\text{Le}^\times$  (grey) compared to the experimental spectrum (red). The theoretical spectrum is a linear combination (0.7beta/0.3alpha) of the two configurations shown in a).

## 6 REFERENCES

- [1] A. Varki, R. D. Cummings, M. Aebi, N. H. Packer, P. H. Seeberger, J. D. Esko, P. Stanley, G. Hart, A. Darvill, T. Kinoshita, *et al.*, *Glycobiology* **2015**, *25*, 1323-1324.
- [2] A. Varki, *Glycobiology* **1993**, *3*, 97-130.
- [3] R. A. Dwek, *Chem. Rev.* **1996**, *96*, 683-720.
- [4] J. M. Berg, J. L. Tymoczko, G. J. Gatto jr., L. Stryer, in *Stryer Biochemie*, Springer, Berlin, Heidelberg, **2018**, pp. 373-403.
- [5] A. Varki, *Cell* **2006**, *126*, 841-845.
- [6] R. B. Myers, S. Srivastava, W. E. Grizzle, *J. Urol.*, *153*, 1572-1574.
- [7] U. University, *Glycoscience: illuminating the secret world of your glycans* [YouTube Video] **2017**, Retrieved 14.03.2018, <https://www.youtube.com/watch?v=sT1qghJZdW8>.
- [8] B. Domon, R. Aebersold, *Science* **2006**, *312*, 212-217.
- [9] J. C. Venter, M. D. Adams, E. W. Myers, P. W. Li, R. J. Mural, G. G. Sutton, H. O. Smith, M. Yandell, C. A. Evans, R. A. Holt, *et al.*, *Science* **2001**, *291*, 1304-1351.
- [10] D. J. Harvey, *Proteomics* **2001**, *1*, 311-328.
- [11] N. Leymarie, J. Zaia, *Anal. Chem.* **2012**, *84*, 3040-3048.
- [12] D. M. Sheeley, V. N. Reinhold, *Anal. Chem.* **1998**, *70*, 3053-3059.
- [13] R. Aebersold, M. Mann, *Nature* **2003**, *422*, 198.
- [14] R. W. Vachet, B. M. Bishop, B. W. Erickson, G. L. Glish, *J. Am. Chem. Soc.* **1997**, *119*, 5481-5488.
- [15] A. G. Harrison, *J. Am. Soc. Mass Spectrom.* **2008**, *19*, 1776-1780.
- [16] R. Chawner, S. W. Holman, S. J. Gaskell, C. E. Eyers, *J. Am. Soc. Mass Spectrom.* **2014**, *25*, 1927-1938.
- [17] A. G. Harrison, *J. Mass Spectrom.* **2014**, *49*, 161-167.
- [18] S. Molesworth, S. Osburn, M. Van Stipdonk, *J. Am. Soc. Mass Spectrom.* **2009**, *20*, 2174-2181.

- 
- [19] A. G. Harrison, A. B. Young, C. Bleiholder, S. Suhai, B. Paizs, *J. Am. Chem. Soc.* **2006**, *128*, 10364-10365.
- [20] C. Jia, Z. Wu, C. B. Lietz, Z. Liang, Q. Cui, L. Li, *Anal. Chem.* **2014**, *86*, 2917-2924.
- [21] I. R. Garcia, K. Giles, R. H. Bateman, S. J. Gaskell, *J. Am. Soc. Mass Spectrom.* **2008**, *19*, 1781-1787.
- [22] X. Chen, L. Yu, J. D. Steill, J. Oomens, N. C. Polfer, *J. Am. Chem. Soc.* **2009**, *131*, 18272-18282.
- [23] U. Erlekam, B. J. Bythell, D. Scuderi, M. Van Stipdonk, B. Paizs, P. Maître, *J. Am. Chem. Soc.* **2009**, *131*, 11503-11508.
- [24] N. C. Polfer, J. Oomens, S. Suhai, B. Paizs, *J. Am. Chem. Soc.* **2007**, *129*, 5887-5897.
- [25] A. A. Goloborodko, M. V. Gorshkov, D. M. Good, R. A. Zubarev, *J. Am. Soc. Mass Spectrom.* **2011**, *22*, 1121-1124.
- [26] I. S. Saminathan, X. S. Wang, Y. Guo, O. Krakovska, S. Voisin, A. C. Hopkinson, K. W. M. Siu, *J. Am. Soc. Mass Spectrom.* **2010**, *21*, 2085-2094.
- [27] A. L. Patrick, N. C. Polfer, in *Gas-Phase IR Spectroscopy and Structure of Biological Molecules* (Eds.: A. M. Rijs, J. Oomens), Springer International Publishing, Cham, **2015**, pp. 153-181.
- [28] M. McNeil, *Carbohydr. Res.* **1983**, *123*, 31-40.
- [29] E. Mucha, A. I. Gonzalez Florez, M. Marianski, D. A. Thomas, W. Hoffmann, W. B. Struwe, H. S. Hahm, S. Gewinner, W. Schollkopf, P. H. Seeberger, *et al.*, *Angew. Chem. Int. Ed.* **2017**, *56*, 11248-11251.
- [30] J. Hofmann, A. Stuckmann, M. Crispin, D. J. Harvey, K. Pagel, W. B. Struwe, *Anal. Chem.* **2017**, *89*, 2318-2325.
- [31] G. P. Moss, P. A. S. Smith, D. Tavernier, *Pure Appl. Chem.* **1995**, *67*, 1307-1375.
- [32] S. Kornfeld, E. Li, I. Tabas, *J. Biol. Chem.* **1978**, *253*, 7771-7778.
- [33] M. Marianski, A. Supady, T. Ingram, M. Schneider, C. Baldauf, *J. Chem. Theory Comput.* **2016**, *12*, 6157-6168.
- [34] H. B. Mayes, L. J. Broadbelt, G. T. Beckham, *J. Am. Chem. Soc.* **2014**, *136*, 1008-1022.
- [35] D. Cremer, J. A. Pople, *J. Am. Chem. Soc.* **1975**, *97*, 1354-1358.

- [36] D. B. Werz, R. Ranzinger, S. Herget, A. Adibekian, C.-W. von der Lieth, P. H. Seeberger, *ACS Chem. Biol.* **2007**, *2*, 685-691.
- [37] L. Bode, *Glycobiology* **2012**, *22*, 1147-1162.
- [38] M. Schneider, E. Al-Shareffi, R. S. Haltiwanger, *Glycobiology* **2017**, *27*, 601-618.
- [39] G. R. Guile, D. J. Harvey, N. O'Donnell, A. K. Powell, A. P. Hunter, S. Zamze, D. L. Fernandes, R. A. Dwek, D. R. Wing, *Eur. J. Biochem.* **1998**, *258*, 623-656.
- [40] D. J. Becker, J. B. Lowe, *Glycobiology* **2003**, *13*, 41R-53R.
- [41] Z. Zhang, P. Sun, J. Liu, L. Fu, J. Yan, Y. Liu, L. Yu, X. Wang, Q. Yan, *BBA - Mol. Cell Res.* **2008**, *1783*, 287-296.
- [42] B. W. T. Yin, C. L. Finstad, K. Kitamura, M. G. Federici, M. Welshinger, V. Kudryashov, W. J. Hoskins, S. Welt, K. O. Lloyd, *Int. J. Cancer* **1996**, *65*, 406-412.
- [43] B. Domon, C. E. Costello, *Glycoconj. J.* **1988**, *5*, 397-409.
- [44] F. Pfrengle, *Curr. Opin. Chem. Biol.* **2017**, *40*, 145-151.
- [45] D. Schmidt, F. Schuhmacher, A. Geissner, P. H. Seeberger, F. Pfrengle, *Chem. Eur. J.* **2015**, *21*, 5709-5713.
- [46] M. Wührer, C. A. M. Koeleman, C. H. Hokke, A. M. Deelder, *Rapid Commun. Mass Spectrom.* **2006**, *20*, 1747-1754.
- [47] M. Wührer, C. A. M. Koeleman, A. M. Deelder, *Anal. Chem.* **2009**, *81*, 4422-4432.
- [48] Y.-L. Ma, I. Vedernikova, H. Van den Heuvel, M. Claeys, *J. Am. Soc. Mass Spectrom.* **2000**, *11*, 136-144.
- [49] D. J. Harvey, T. S. Mattu, M. R. Wormald, L. Royle, R. A. Dwek, P. M. Rudd, *Anal. Chem.* **2002**, *74*, 734-740.
- [50] A. H. Franz, C. B. Lebrilla, *J. Am. Soc. Mass Spectrom.* **2002**, *13*, 325-337.
- [51] B. Ernst, D. R. Müller, W. J. Richter, *Int. J. Mass Spectrom. Ion Process.* **1997**, *160*, 283-290.
- [52] V. Kováčik, J. Hirsch, P. Kováč, W. Heerma, J. Thomas-Oates, J. Haverkamp, *J. Mass Spectrom.* **1995**, *30*, 949-958.
- [53] L. P. Brüll, W. Heerma, J. Thomas-Oates, J. Haverkamp, V. Kováčik, P. Kovác, *J. Am. Soc. Mass Spectrom.* **1997**, *8*, 43-49.



- 
- [54] L. P. Brüll, V. Kováčik, J. E. Thomas-Oates, W. Heerma, J. Haverkamp, *Rapid Commun. Mass Spectrom.* **1998**, *12*, 1520-1532.
- [55] F. W. McLafferty, *Anal. Chem.* **1959**, *31*, 82-87.
- [56] E. S. Hecht, P. L. Loziuk, D. C. Muddiman, *J. Am. Soc. Mass Spectrom.* **2017**, *28*, 729-732.
- [57] C. Nwosu, H. K. Yau, S. Becht, *Anal. Chem.* **2015**, *87*, 5905-5913.
- [58] N. Desai, D. A. Thomas, J. Lee, J. Gao, J. L. Beauchamp, *Chem. Sci.* **2016**, *7*, 5390-5397.
- [59] A. M. Rijs, J. Oomens, in *Gas-Phase IR Spectroscopy and Structure of Biological Molecules* (Eds.: A. M. Rijs, J. Oomens), Springer International Publishing, Cham, **2015**, pp. 1-42.
- [60] M. Okumura, L. I. Yeh, Y. T. Lee, *J. Chem. Phys.* **1985**, *83*, 3705-3706.
- [61] N. Khanal, C. Masellis, M. Z. Kamrath, D. E. Clemmer, T. R. Rizzo, *Anal. Chem.* **2017**, *89*, 7601-7606.
- [62] C. Masellis, N. Khanal, M. Z. Kamrath, D. E. Clemmer, T. R. Rizzo, *J. Am. Soc. Mass Spectrom.* **2017**, 2217-2222.
- [63] M. Z. Kamrath, E. Garand, P. A. Jordan, C. M. Leavitt, A. B. Wolk, M. J. Van Stipdonk, S. J. Miller, M. A. Johnson, *J. Am. Chem. Soc.* **2011**, *133*, 6440-6448.
- [64] N. Khanal, C. Masellis, M. Z. Kamrath, D. E. Clemmer, T. R. Rizzo, *Analyst* **2018**.
- [65] A. I. Gonzalez Florez, D. S. Ahn, S. Gewinner, W. Schollkopf, G. von Helden, *Phys. Chem. Chem. Phys.* **2015**, *17*, 21902-21911.
- [66] S. Goyal, D. L. Schutt, G. Scoles, *Phys. Rev. Lett.* **1992**, *69*, 933-936.
- [67] A. Lindinger, J. P. Toennies, A. F. Vilesov, *J. Chem. Phys.* **1999**, *110*, 1429-1436.
- [68] F. Bierau, P. Kupser, G. Meijer, G. von Helden, *Phys. Rev. Lett.* **2010**, *105*, 133402.
- [69] A. I. Gonzalez Florez, E. Mucha, D. S. Ahn, S. Gewinner, W. Schollkopf, K. Pagel, G. von Helden, *Angew. Chem. Int. Ed.* **2016**, *55*, 3295-3299.
- [70] A. I. Gonzalez Florez, PhD thesis, Freie Universität (Berlin), **2016**.
- [71] F. Filsinger, D.-S. Ahn, G. Meijer, G. von Helden, *Phys. Chem. Chem. Phys.* **2012**, *14*, 13370-13377.

- [72] W. Schöllkopf, S. Gewinner, H. Junkes, A. Paarmann, G. von Helden, H. Bluem, A. M. M. Todd, in *Proc. of SPIE - Advances in X-ray Free-Electron Lasers Instrumentation III*, Vol. 9512 (Ed.: S. G. Biedron), Prague, Czech Republic, **2015**.
- [73] S. Warnke, G. von Helden, K. Pagel, *Proteomics* **2015**, *15*, 2804-2812.
- [74] M. Wührer, A. M. Deelder, Y. E. M. van der Burgt, *Mass Spectrometry Reviews* **2011**, *30*, 664-680.
- [75] S. Krimm, J. Bandekar, in *Adv. Protein Chem.*, Vol. 38 (Eds.: C. B. Anfinsen, J. T. Edsall, F. M. Richards), Academic Press, **1986**, pp. 181-364.
- [76] A. Barth, C. Zscherp, *Q. Rev. Biophys.* **2003**, *35*, 369-430.
- [77] S. Re, S. Watabe, W. Nishima, E. Muneyuki, Y. Yamaguchi, A. D. MacKerell, Y. Sugita, *Sci. Rep.* **2018**, *8*, 1644.
- [78] E. P. L. Hunter, S. G. Lias, *J. Phys. Chem. Ref. Data* **1998**, *27*, 413-656.
- [79] A. L. L. East, B. J. Smith, L. Radom, *J. Am. Chem. Soc.* **1997**, *119*, 9014-9020.
- [80] S. S. Uppal, S. E. Beasley, M. Scian, M. Guttman, *Anal. Chem.* **2017**, *89*, 4737-4742.

## 7 APPENDIX

## MASS SPECTRA WITH DIFFERENT SOURCE CONDITIONS

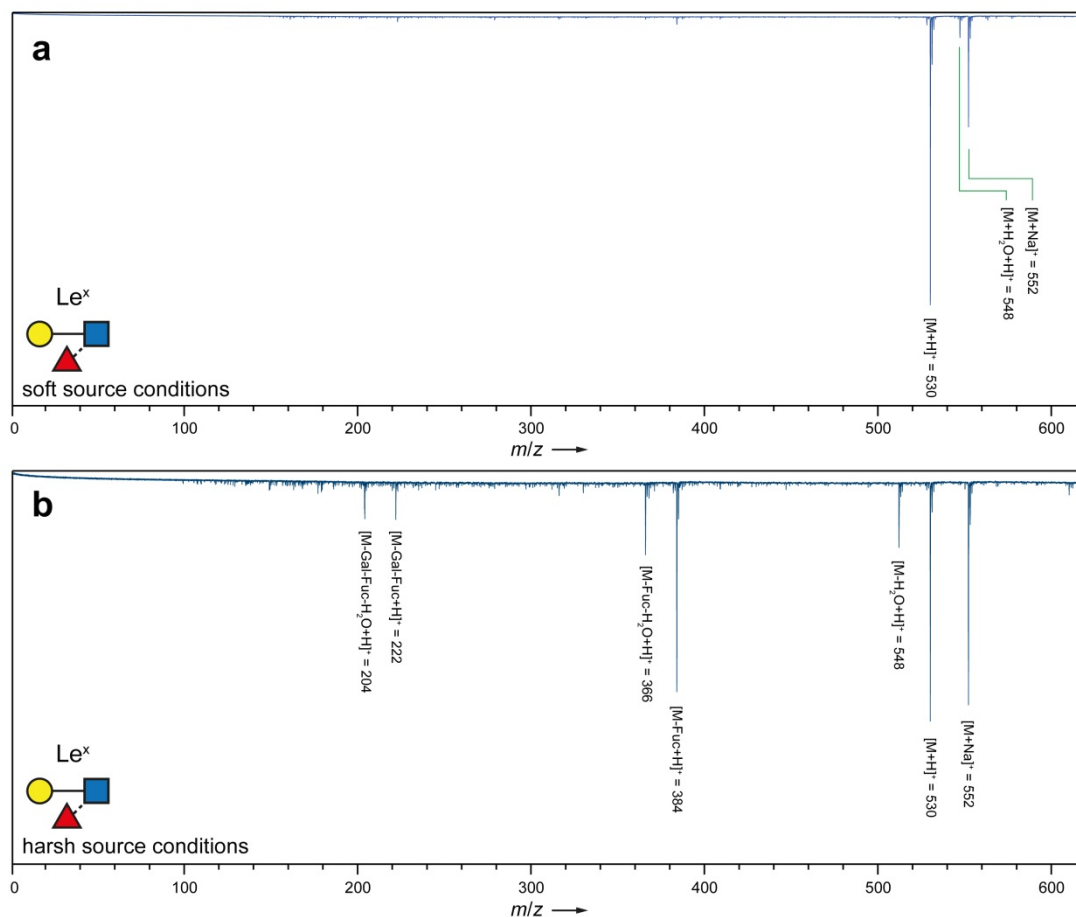
Le<sup>x</sup> Trisaccharide

Figure 32: MS spectra for Le<sup>x</sup> at a) soft source conditions and b) harsh source conditions. Soft source conditions were utilized to investigate the intact trisaccharide ions.

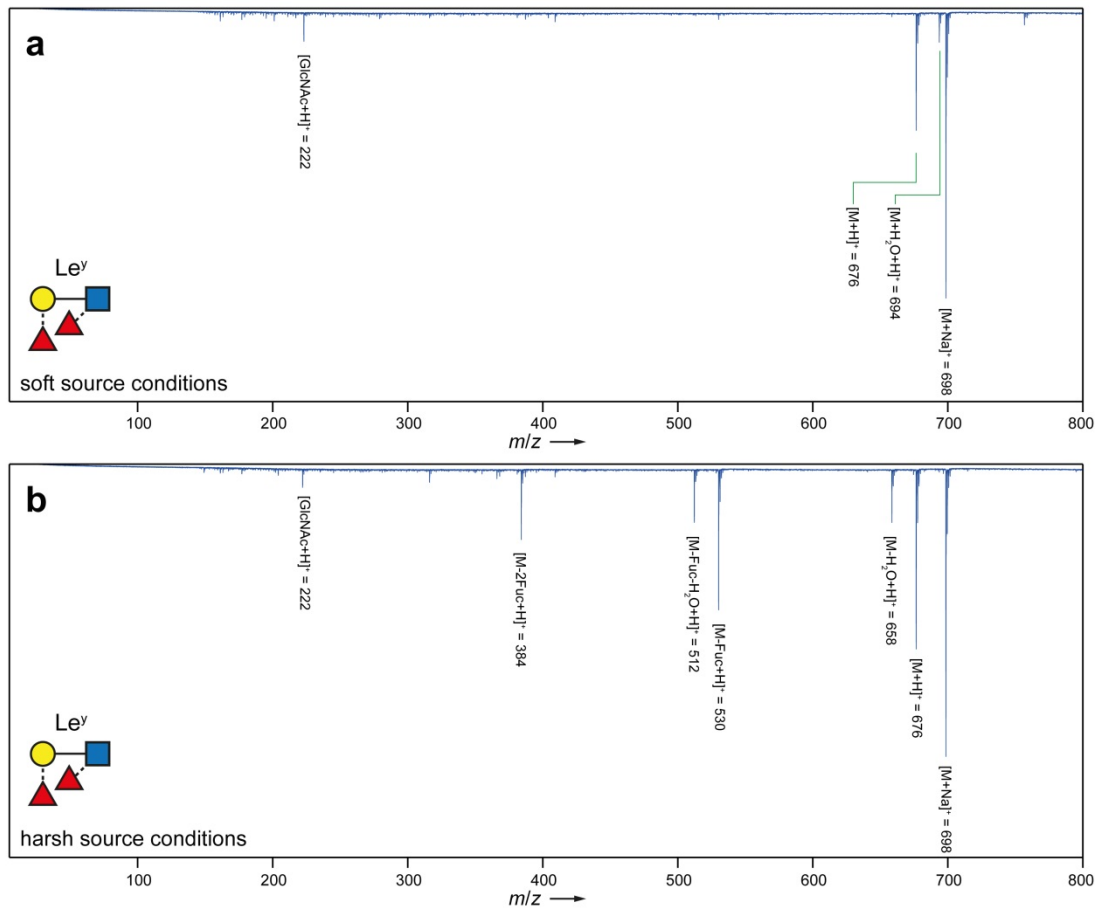
Le<sup>y</sup> Tetrasaccharide

Figure 33: MS spectra for Le<sup>y</sup> at a) soft source conditions and b) harsh source conditions. Harsh source conditions were utilized to investigate the fragmented tetrasaccharide.

## TANDEM MS SPECTRA

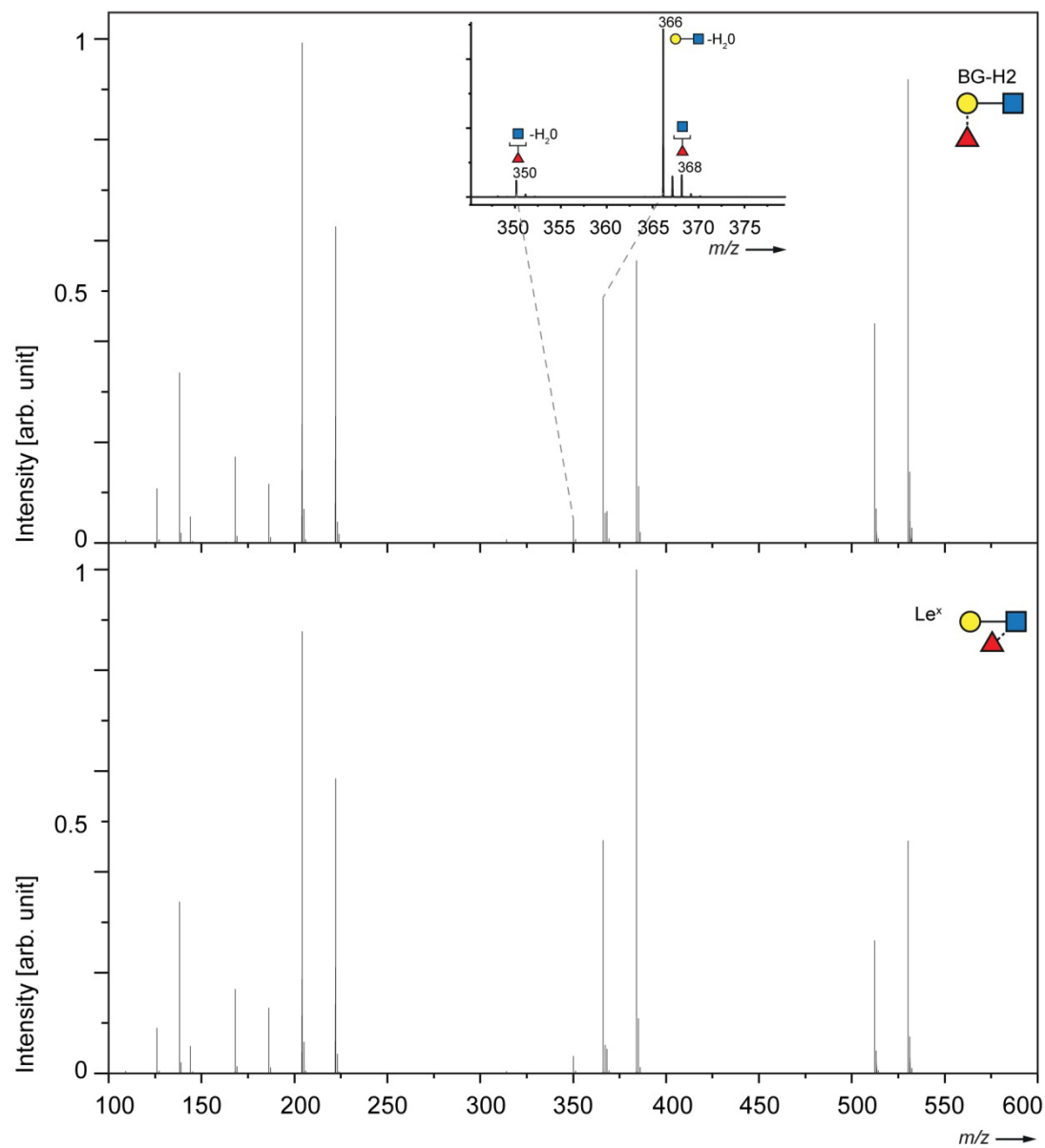
BG-H2 and Le<sup>x</sup>

Figure 34: Tandem MS spectra of BG-H2 (upper panel) and Le<sup>x</sup> (lower panel) with a mass-to-charge selection of  $m/z$  530 which is the  $[M+H]^+$  parent ion and CID. Migration products are indirectly detectable as IRL fragment for BG-H2.

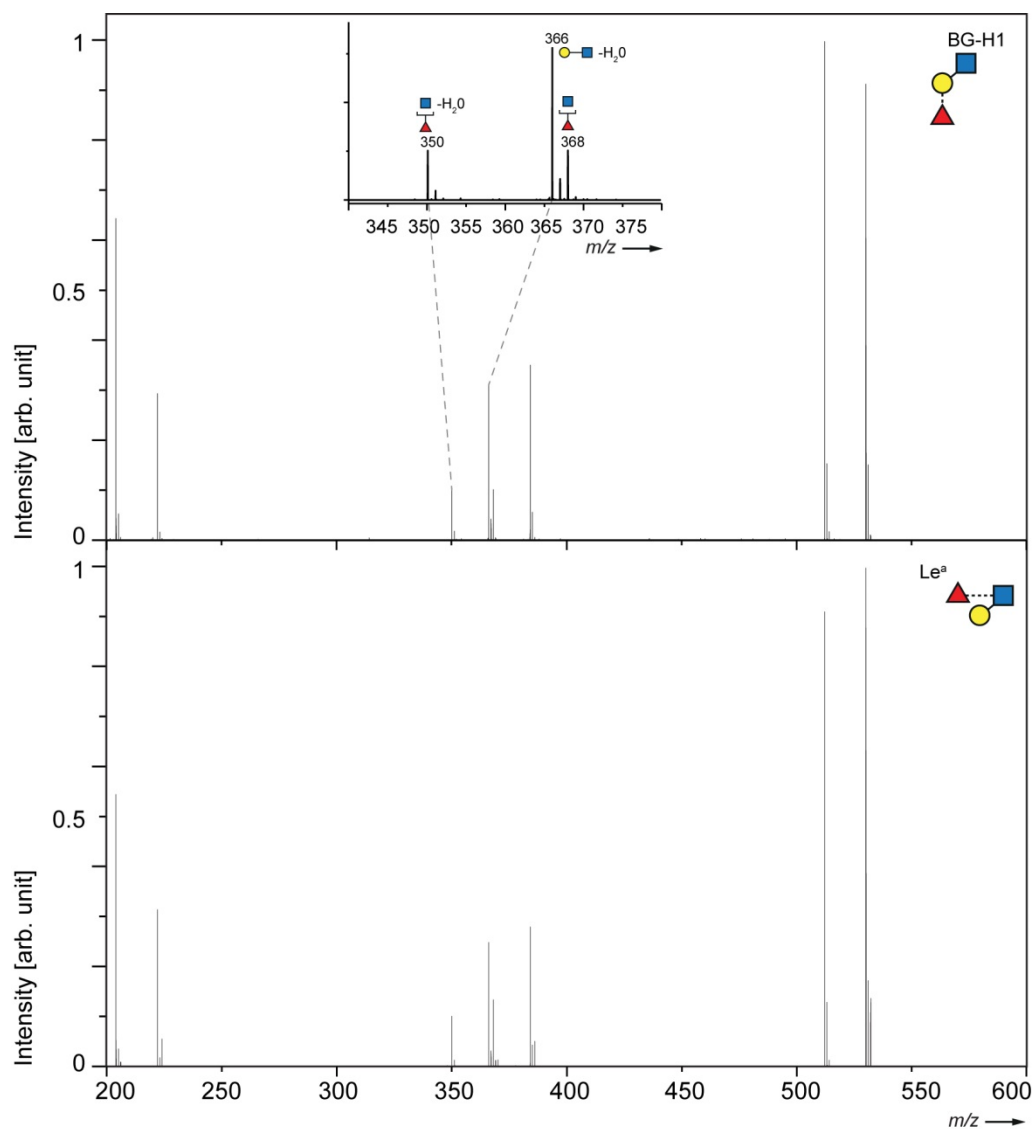
BG-H1 and Le<sup>a</sup>

Figure 35: Tandem MS spectra of BG-H1 (upper panel) and Le<sup>a</sup> (lower panel) with a mass-to-charge selection of  $m/z$  530 which is the [M+H]<sup>+</sup> parent ion and CID. Migration products are indirectly detectable as IRL fragment for BG-H1.

## CALCULATED IR SPECTRA

## Protonated Trimethylammonia

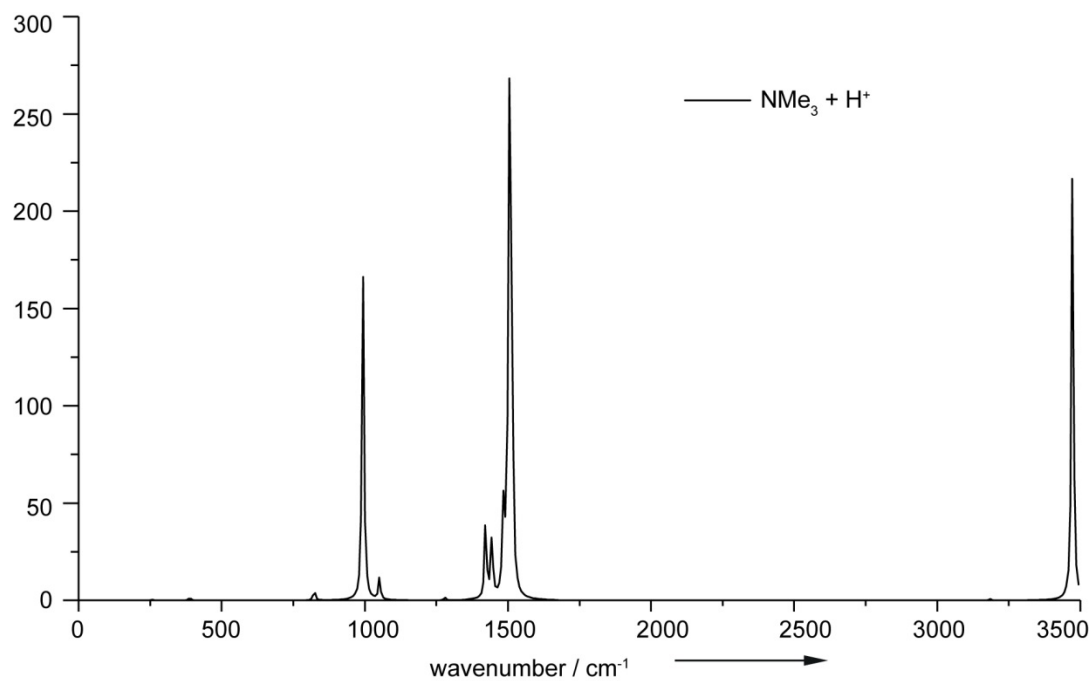


Figure 36: Calculated IR Spectrum of protonated trimethylammonia (pbe1pbe/aug-cc-pVTZ).

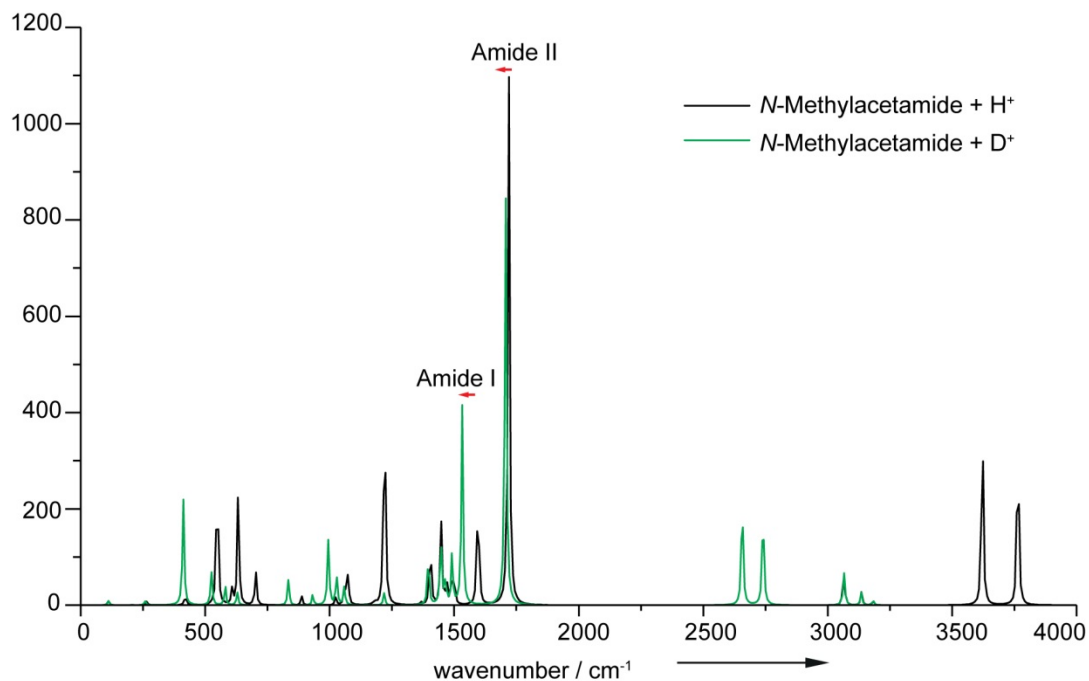
Protonated and Deuterated *N*-Methylacetamide

Figure 37: Overlay of the calculated IR Spectra of protonated *N*-methylacetamide and deuterated *N*-methylacetamide (a deuterium at the nitrogen and a deuterium at the oxygen) (pbe1pbe/aug-cc-pVTZ). Red arrows indicate the shift of the amide I and amide II vibration.



## STATUTORY DECLARATION

Hiermit versichere ich, Maike Lettow, Matrikelnummer 4729614, geboren am 17.07.1990 in Brunsbüttel, an Eides statt, dass die vorliegende Arbeit von mir selbstständig und ohne unerlaubte Hilfe Dritter verfasst wurde und ich keine anderen als die angegebenen Quellen und Hilfsmittel verwendet sowie wörtliche und sinngemäße Zitate als solche kenntlich gemacht habe.

Diese Arbeit hat in gleicher oder ähnlicher Form noch keiner anderen Prüfungsbehörde vorgelegen und wurde bisher nicht veröffentlicht.

Ort, Datum

Unterschrift